CT-TDLAS measurements of gas concentration and temperature distributions in a semiconductor chamber

（CT-TDLAS による半導体チャンバ内のガス濃度・温度分布測定）

March, 2020

Graduate School of Advanced Technology and Science

Intelligent Structures and Mechanics Systems Engineering

Mechanical Engineering

Daisuke Hayashi

Contents

Chapter 1 Introduction · 3

1.1 Recent trend on semiconductor process

1.2 Significance of semiconductor process monitoring with CT-TDLAS

1.3 Article structure

Chapter 2 Theoretical background · 6

2.1 Tunable diode laser absorption spectroscopy (TDLAS)

2.2 Computed tomography (CT)

2.3 CT-TDLAS algorithm

2.4 Fast processing of CT-TDLAS calculation

Chapter 3 Calibration of CH_4 measurement system and database construction · · · · · · · · · · 12

Chapter 4 Design of CT-TDLAS chamber for semiconductor process · · · · · · · · · · · · · · 16

4.1 CT-TDLAS measurement system

4.2 Chamber structure

Chapter 5 Validity checks of CT algorithm · 20

5.1 Validation of concentration distribution algorithm using concentric cylinder

5.2 Spatial resolution of reconstructed distribution

5.3 Validation of algorithm for concentration and temperature distributions using computer fluid dynamics

Chapter 6 CT-TDLAS measurements of CH_4 concentration and temperature distributions in chamber · 32

6.1 Experimental system

6.2 Concentration distribution measurement

6.3 Simultaneous measurement of concentration and temperature distributions

Chapter 7 Conclusion · 39

References · 41

Acknowledgment · 49

Chapter 1 Introduction

1.1 Recent trend of semiconductor process

In recent years, semiconductor devices have been highly integrated. Large scale transistors with complicated fine structures like the three-dimensional NOT-AND flash memories [1] or the fin field effect transistors [2, 3, 4] are being manufactured in mass production phase. For the productions of these devices, precise etchings and depositions to realize fine structures including nanoscale critical dimensions (CDs) and high aspect ratio trenches are essential. In particular, the dry etching plays considerably important roles because the most of the fine structures are formed through this process, and the electric properties of the devices are directly affected by the quality of the process [5, 6]. From the generation of the 90-nm node devices or later, etchings for dimensions smaller than resist mask patterns have been required. Therefore, many process engineers have been trying to improve the quality of the dry etching.

In the dry etching, seed gases are decomposed by plasma in chambers, and highly reactive molecules or atoms are fed on wafers. For example, in the case of Si etchings, halogen atoms are fed on the surface of a Si wafer to create a reformed layer having low boiling point, such as $Si+4F \rightarrow SiF_4$. On the other hand, positively charged ions like Ar^+ produced in plasma are irradiated toward the surface layers, then the reformed layers are removed. As the positive ions are accelerated by the plasma sheath, which is an electric field between the plasma and the wafer, the ions vertically attack the wafer surface. Throughout this process, anisotropic etchings proceed and precise fabrications loyal to mask patterns are realized. This type of dry etching is called as the reactive ion etching (RIE), which has been widely used for a long time as a conventional etching method. With increasing the integration densities, fabrications for CDs less than 10 nm have become required for the dry etching recently. As the results, atomic layer etching (ALE) has been implemented [7, 8, 9, 10, 11, 12, 13, 14]. The ALE has temporally separated two steps: the adsorption step, in which atoms excited by plasma are adsorbed on a surface layer to create a reformed layer, and the removal

step, in which the reformed layer is removed by ion bombardments. These two steps are alternately repeated. In the former step, the adsorption is made only for a single atomic layer, and no more adsorption proceeds even if excessive atoms are fed. In the latter step, the ion energy are adjusted so that only the reformed single atomic layer is removed. This type of reaction is called as "the self-limiting reaction," which allows atomic size etchings. (In the case the self-limiting reaction is applied for depositions, the process is called the atomic layer deposition [15].) For both the RIE and ALE, highly precise controls of plasma, gas concentration, and temperature in the chamber by tuning external parameters are required. To realize the controls, measurement technologies to monitor the chamber in-situ have critically important meanings.

1.2 Significance of semiconductor process monitoring with CT-TDLAS

The dry etching includes some serious difficulties, one of which is that the CDs are not uniform across a wafer processed with non-uniform spatial distributions of gas concentration, temperature, and plasma sheath intensity [16, 17, 18, 19]. Their conditions at the center of wafers are different from at vicinities of chamber walls, and the differences cause the CD non-uniformity or unexpected fabrications like trench tiltings. As the results, device performances or yielding rates are degraded. The CD uniformity has been improved to some extent by precisely tuning the temperature distribution on a multi-zone electrostatic chuck [20, 21, 22] or applying virtual metrologies [23, 24, 25, 26]. On the other hand, the CD uniformity in the ALE is considered to be less sensitive to the spatial distributions compared to the RIE [27, 28, 29, 30, 31, 32]. The quality of the dry etching has been gradually refined with these technologies. However, the improvement of CD uniformity has not yet achieved to get sufficient yielding rates in mass productions. In addition, although tuning parameters to get optimal process conditions is extremely difficult and time-consuming, the conditions in the chamber can drift during the process or run-to-run repetitions [33, 34, 35]. Therefore, to achieve the optimal conditions in the chamber and keep them stably as long as possible, the technology to measure the spatial distributions is strongly desired.

This work proposes the way to measure conditions inside chamber and tune parameters in-situ. Tunable diode laser absorption spectroscopy (TDLAS) is a useful method for the chamber in-situ measurement in a non-contact manner [36, 37]. In the TDLAS, absorption spectra of trace gas are measured using near-infrared (NIR) [38] or mid-infrared (MIR) [39, 40, 41, 42, 43, 44, 45, 46, 47, 48] laser light sources, and the gas concentration and temperature [49] can be determined. Applications of the TDLAS for plasma diagnostics in chambers were reported [50, 51]. In-situ monitoring which focused on the dry etching were also performed, where trends of concentration of gas species [52] or plasma radicals [53, 54] were measured. However, as the TDLAS generally utilizes a single laser path in the measured area and collects just one absorption spectrum integrated over the laser path, it cannot measure the spatial distributions of gas concentration or temperature. To measure the spatial distributions in a chamber, computed tomography-tunable diode laser absorption spectroscopy (CT-TDLAS) can be a promising candidates [55, 56, 57, 58, 59]. In this method, infrared absorption spectra for multiple laser paths passing through a measured area are collected. Based on the spectra, the spatial distributions of gas concentration and temperature are reconstructed with the numerical calculation of the computed tomography (CT). This method has been adopted for analyses of combustion fields [60, 61, 62, 63, 64, 65, 66], vehicle engine exhausts [67, 68] and diagnosis of an aero-propulsion engine [69]. Recently, expansions to the three-dimensional tomography have been studied [70, 71, 72]. However, an application for measurement in a semiconductor chamber has not been reported except for our works [73, 74]. The inner space of the semiconductor chamber is a closed system, and the behaviors of temperature and pressure are considered to be different from those of engine or combustion fields.

1.3 Article structure

In this work, the CT-TDLAS was applied to measure CH_4 concentration and temperature distributions simultaneously in our designed experimental semiconductor process chamber. To focus on the basic

investigation of the CT-TDLAS applicability to the semiconductor chamber, the gas species and the chamber pressure employed in the examinations were limited to CH_4 and 760 Torr, respectively. In Chapter 2, theoretical background of the CT-TDLAS including the details of the CT algorithm is reviewed. In Chapter 3, construction of CH_4 spectrum database required for the CT-TDLAS measurements is described. In Chapter 4, the CT-TDLAS measurement system and structure of our designed semiconductor chamber in which the CT-TDLAS system is installed are shown. In Chapter 5, the validity of the CT-TDLAS measurements and the algorithm was checked using a simple experiment with a five-fold concentric cylinder and simulations of the computer fluid dynamics (CFD). In Chapter 6, CH_4 was actually fed into the chamber to measure the concentration and temperature distributions with the CT-TDLAS. Then the meanings of the measured results are discussed.

Chapter 2 Theoretical background

2.1 Tunable diode laser absorption spectroscopy (TDLAS)

The principle of TDLAS is based on the Lambert-Beer's law. When a light signal passes through a media, the light intensity is attenuated due to absorption. The absorbance A at a wavelength λ is defined as:

$$\mathrm{A}(\lambda) = \log\left(\frac{I_0(\lambda)}{I(\lambda)}\right). \tag{1}$$

Here $I_0(\lambda)$ and $I(\lambda)$ are an incident and transmitted light intensity, respectively. In the case of a single gas species is present, the absorbance is related to the concentration C as follows [75, 76, 77, 78, 79, 80]:

$$A(\lambda) = CLP\sum_{j\in\lambda} S_j(T)G_{vj}\,. \tag{2}$$

Here L is the path length, P is the pressure, $S_j(T)$ is the absorption line strength of transition j at temperature$T$, and G_{vj} is the line broadening function, which is usually approximated by the Voigt function.

Under a fixed temperature, the absorbance of the species is proportional to its concentration. Meanwhile, the absorption line strength depends on temperature as

$$S_j(T) = S_j(T_0)\frac{Q(T_0)}{Q(T)}\frac{T_0}{T}\exp\left[-\frac{hcE_j}{k}\left(\frac{1}{T}-\frac{1}{T_0}\right)\right]\frac{1-\exp\left(\frac{hc\nu_{0j}}{k_B T}\right)}{1-\exp\left(\frac{hc\nu_{0j}}{k_B T_0}\right)}, \tag{3}$$

where T_0 is a reference temperature, $Q(T)$ is the partition function, E_j is the lower-state energy of the transition, ν_{0j} is the line center frequency, h is Planck's constant, c is the speed of light, and k_B is Boltzmann's constant [81, 82, 83]. As the line strength of each transition has different temperature dependence, the absorption spectrum including more than two absorption wavelengths can be used to measure the gas temperature as well as concentration.

2.2 Computed tomography (CT)

The computed tomography (CT) is an image reconstruction method, in which optical beam is irradiated to a target object from various directions and the image of the inner states such as gas concentration and temperature distributions are reconstructed through the numerical calculation based on the absorption spectra. The X-ray CT is well known in the medical fields. In the X-ray CT, an X-ray source is mechanically scanned around the target to get the image of cross section [84]. On the other hand, in the CT-TDLAS studied in this work, the NIR laser is used as a light source and the multiple beam injection ports are fixed around the measured. Multiple laser paths are intersected with each other to form analysis grids in the measured area, and the integrated absorbance $A_p^{(meas)}(\lambda)$ is acquired for each path. (p is the path index.) Whereas, when the concentration and temperature distributions are given, the integrated absorbance $A_p^{(cal)}(\lambda)$ is calculated by

$$A_p^{(cal)}(\lambda) = \int_{(x,y)\in p} C(x,y)\alpha\big(\lambda, T(x,y)\big)dl, \tag{4}$$

where $C(x, y)$ and $T(x, y)$ are concentration and temperature at a grid (x, y), and α is the absorbance per unit concentration per unit length. $C(x, y)$ and $T(x, y)$ are determined so that the square error defined as

$$E = \sum_p \int \left\{ A_p^{(cal)}(\lambda) - A_p^{(meas)}(\lambda) \right\}^2 d\lambda \tag{5}$$

is minimized.

2.3 CT-TDLAS algorithm

The procedure of the CT calculation is as follows:

(i) Arbitrary distributions of concentration and temperature are given as the initial distributions.

(ii) The distributions are approximated in the form of polynomials as

$$C(x, y) = \sum_{l>m} a_{lm} x^{l-m} y^m, \tag{6}$$

$$T(x, y) = \sum_{l>m} b_{lm} x^{l-m} y^m. \tag{7}$$

Here l, m are the polynomial order.

(iii) The integrated absorbance $A_p^{(cal)}(\lambda)$ along each path is calculated for the given distribution. In the practical calculation, the integral in Eq. (4) is replaced with a sum with respect to the grids belonging to the path p as

$$A_p^{(cal)}(\lambda) = \sum_q C_q \alpha(\lambda, T_q) \Delta L_{pq} , \tag{8}$$

where C_q, T_q are respectively the concentration and temperature in grid q, ΔL_{pq} is the distance between adjacent grids in path p.

(iv) The square error E is calculated from Eq. (5). (If it is difficult to calculate E due to the baseline shifts in the measured spectrum, the polynomial noise reduction technique is effective in eliminating the shifts [85].)

(v) If the square error is not minimized, the distributions are updated so that the square error is decreased in the manner of the gradient method, i.e., they are changed to follow the steepest descent direction in the E with respect to $\{a_{lm}\}$ and $\{b_{lm}\}$,

$$a_{lm} := a_{lm} - \eta \frac{\partial E}{\partial a_{lm}}, \tag{9}$$

$$b_{lm} := b_{lm} - \eta \frac{\partial E}{\partial b_{lm}}, \tag{10}$$

where η is a small parameter called the learning rate.

The steps of (ii)-(v) are iterated until the square error reaches the minimum. The proper value of η is commonly determined through trial and errors at around $1.0 \times 10^{-3} \sim 10^{-5}$. In this work, $\eta = 1.0 \times 10^{-4}$ was employed. The criteria to finish the calculation was that $E < 0.1$ and $|\Delta E|/E < 1.0 \times 10^{-5}$ (ΔE is the variation of E per cycle). This η value and the criteria allowed the calculation to be finished within several seconds. The outline of the procedure is summarized in Fig. 1.

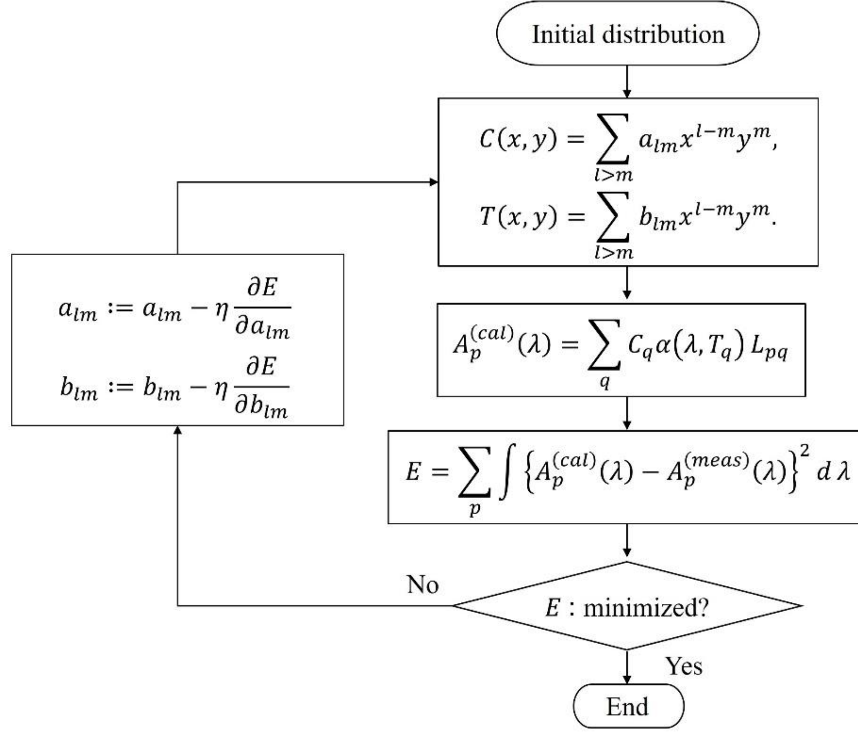

Fig. 1 Flow chart of the CT calculation.

2.4 Fast processing of CT-TDLAS calculation

To achieve the target distributions with the minimum square error for a short calculation period, setting the initial distributions as close to the target is important. One useful method is to use the path averaged concentrations and temperatures calculated from the measured spectra. First, the initial distributions are set as linear combinations of arbitrary distribution patterns [68]

$$C^{(ini)}(x,y,\vec{u}) = \sum_k u_k C^{(k)}(x,y), \tag{11}$$

$$T^{(ini)}(x,y,\vec{v}) = \sum_k v_k T^{(k)}(x,y), \tag{12}$$

where $C^{(k)}(x,y)$, $T^{(k)}(x,y)$ are distribution patterns (k is the index of the pattern), and $\vec{u} = (u_0, u_1, \cdots), \vec{v} = (v_0, v_1, \cdots)$ are the weight coefficient vectors. In this study, thirty-five distribution

patterns shown in Fig. 2 were employed for setting $C^{(k)}(x, y)$ and $T^{(k)}(x, y)$.

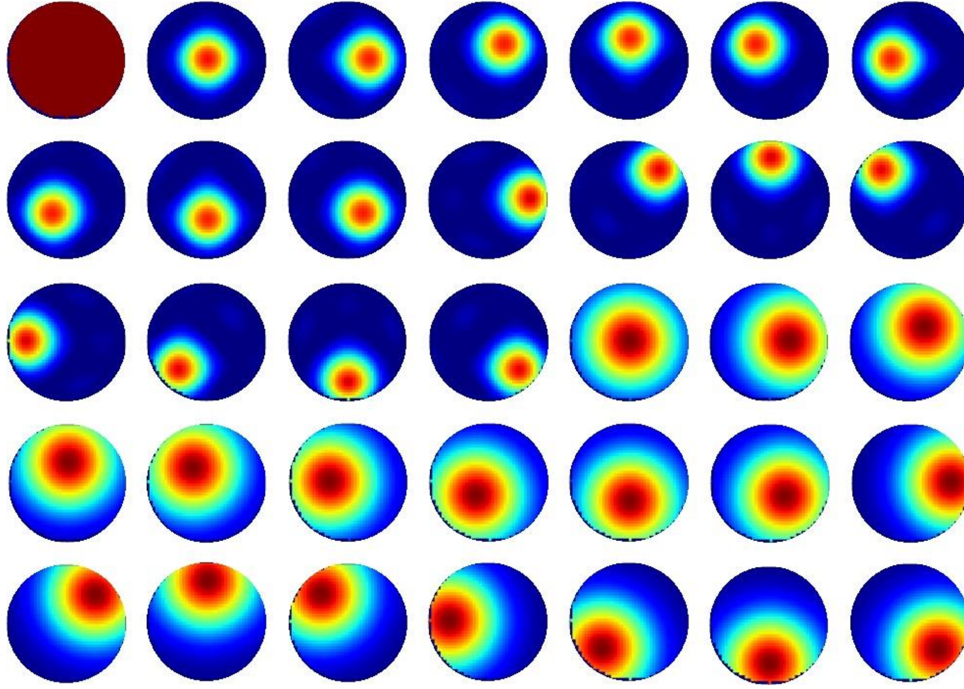

Fig. 2 Patterns for setting initial distributions.

Next, the measured path averages $\bar{C}_p^{(meas)}$, $\bar{T}_p^{(meas)}$ were determined to satisfy the measured absorbance as,

$$A_p^{(meas)}(\lambda) = \bar{C}_p^{(meas)} \alpha\left(\lambda, P, \bar{T}_p^{(meas)}\right) L_p. \tag{13}$$

Here L_p is the length of path p. The square differences between $\bar{C}_p^{(meas)}$ and $\bar{C}_p^{(ini)}$, $\bar{T}_p^{(meas)}$ and $\bar{T}_p^{(ini)}$ are respectively expressed as

$$E^C = \sum_p \left(\bar{C}_p^{(meas)} - \bar{C}_p^{(ini)}(x, y, \vec{u})\right)^2, \tag{14}$$

$$E^T = \sum_p \left(\bar{T}_p^{(meas)} - \bar{T}_p^{(ini)}(x, y, \vec{v})\right)^2. \tag{15}$$

The weight coefficient vectors $\vec{u}$ and $\vec{v}$ were determined to minimize E^C and E^T, respectively, i.e.,

$$\frac{\partial E^C}{\partial u_k} = 0, \tag{16}$$

$$\frac{\partial E^T}{\partial v_k} = 0. \tag{17}$$

In this procedure, the iterative calculation used in the CT is not necessary. Therefore, it takes little time to get the suitable initial distributions.

Chapter 3 Calibration of CH_4 measurement system and database construction

CH_4 has many absorption peaks in the NIR region. Figure 3 shows CH_4 absorption spectrum in the NIR region appeared in HITRAN Database [86]. We focused on the peaks of $\lambda = 1628.1$ nm and 1653.7 nm to measure CH_4 concentration and temperature. Distributed feedback laser diodes (DFB-LDs) at 1628 nm and 1654 nm (NTT Electronics Co., NLK1U5EAAA) were used as the laser sources. Figures 4 and 5 illustrate the wavelength characteristics regarding applied current and temperature of the two LDs. By adjusting the temperatures, the lasing wavelengths can be scanned around the CH_4 absorption wavelengths with the current modulation. In this study, we set 12.7 °C for 1628-nm LD and 11.5 °C for 1654-nm LD, and modulated the current at 0-300 mA.

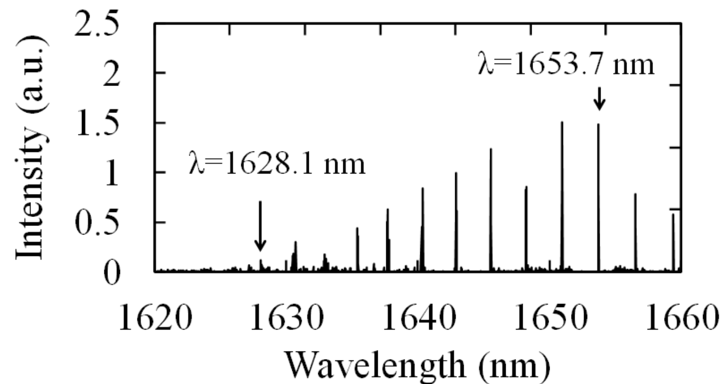

Fig. 3 CH_4 absorption spectrum in the near-infrared region.

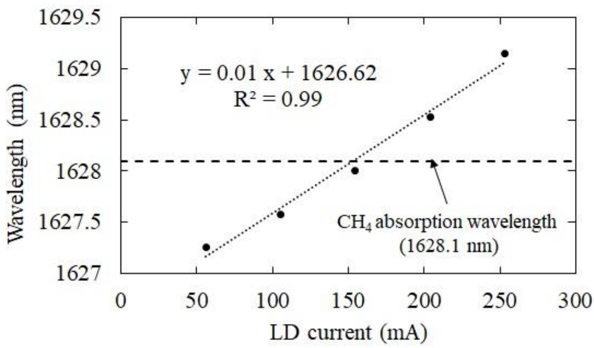

(a) 1628-nm LD

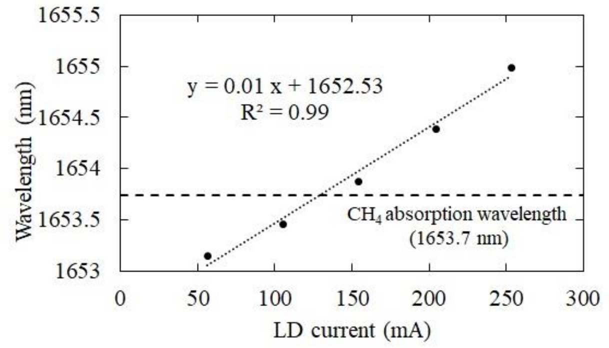

(b) 1654-nm LD

Fig. 4 Wavelength versus applied current characteristics of the LDs. Dashed lines show CH_4 absorption wavelengths (1628.1 nm and 1653.7 nm). LD temperature was fixed at 15 °C.

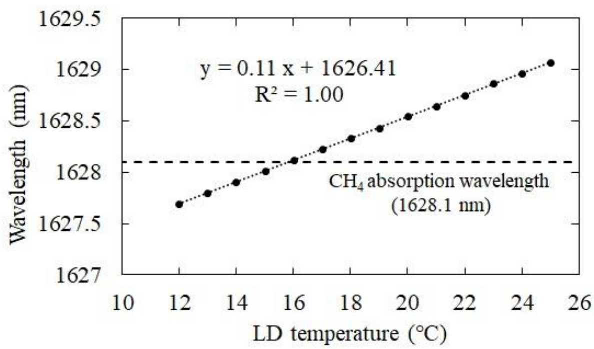

(a) 1628-nm LD

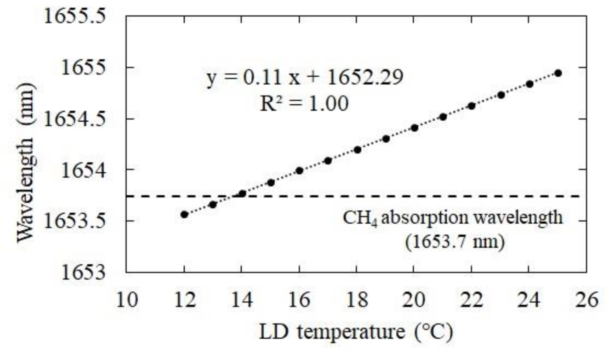

(b) 1654-nm LD

Fig. 5 Wavelength versus temperature characteristics of the LDs. Dashed lines show CH_4 absorption wavelengths (1628.1 nm and 1653.7 nm). LD current was fixed at 150 mA.

CH_4 spectra were acquired to construct a database of $\alpha(\lambda, T)$ using the acquisition system. Figure 6 shows the CH_4 spectrum acquisition system. CH_4 was introduced into a gas cell equipped in a temperature-controlled heating furnace. Laser beam emitted from the LDs was injected into the cell. The length of the gas cell was 102 mm. The pressure in the cell was regulated with a pressure gauge and a control valve placed at downstream. The beam passing through the gas cell was detected by a photodiode (PD,

Hamamatsu, G12180-010SPL). The linearity of the absorbance for various CH_4 concentrations was checked under the fixed pressure (760 Torr) and temperature (27 °C). A Good linearity was confirmed shown in Fig. 7.

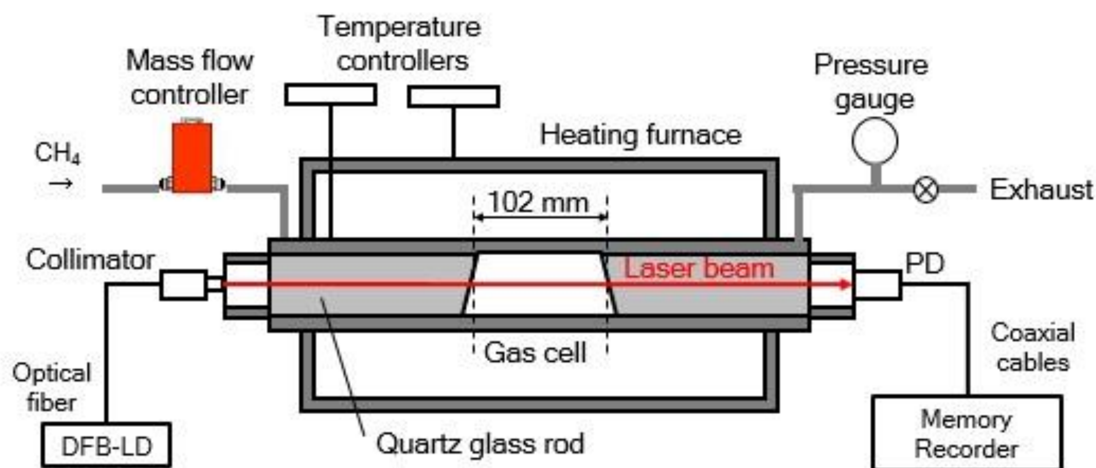

Fig. 6 CH_4 spectrum acquisition system. The edges of the quartz glass rods were shaped like wedges to avoid optical interference caused by multiple reflections.

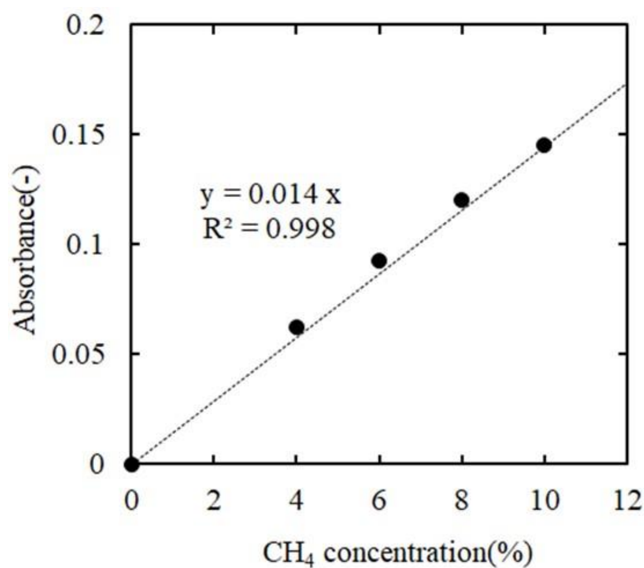

Fig. 7 Linearity check of the CH_4 spectrum acquisition system. The cell length, pressure, temperature were 102 mm, 760 Torr, and 27 °C, respectively.

The spectrum was acquired under various cell pressures (100, 200, 300, 400, 500, 600, 760 Torr) and temperatures (300, 400, 500, 600, 700, 773 K). The absorbance was normalized as the one per unit concentration (1%) per unit cell length (1 cm). Some examples of the acquired spectrum are shown in Fig. 8.

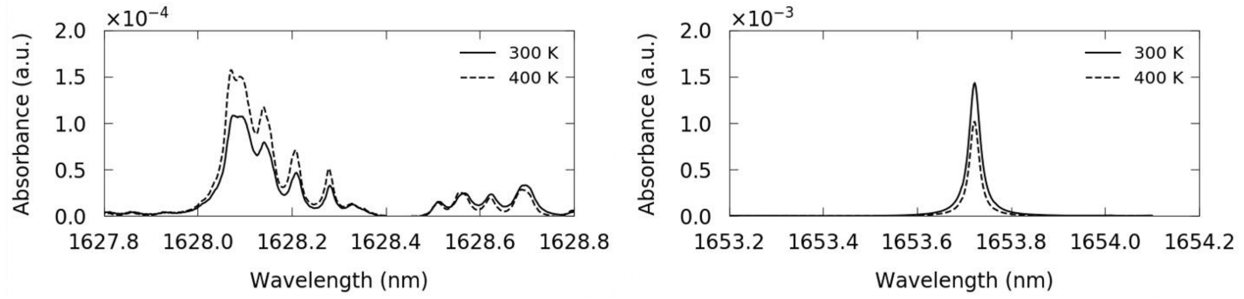

Fig. 8 Examples of acquired CH_4 spectrum around (a) 1628.1 nm and (b) 1653.7 nm. The absorbance was normalized as the one per unit concentration (1%) and unit cell length (1 cm).

To obtain the spectrum for an arbitrary condition of temperature and pressure, measured spectra $A^{meas}(\lambda)$ were approximated as,

$$A^{approx}(\lambda) = \sum_{c} I_c \ V_{R,w_v,\lambda_c}(\lambda), \tag{18}$$

where I_c is the peak intensity of the absorption having the center wavelength λ_c, and $V_{R,w_v,\lambda_c}(\lambda)$ is the pseudo-Voigt function defined as

$$\begin{aligned} V_{R,w_v,\lambda_c}(\lambda) &= (1-R)\exp\left(-2.772\left(\frac{\lambda-\lambda_c}{W_v}\right)^2\right) + \frac{R}{1+4\left(\frac{\lambda-\lambda_c}{W_v}\right)^2} \\ &\quad +0.016(1-R)R\left\{\exp\left(-0.4\left|\frac{\lambda-\lambda_c}{W_v}\right|^{2.25}\right) - \frac{10}{10+4\left|\frac{\lambda-\lambda_c}{W_v}\right|^{2.25}}\right\}, \end{aligned} \tag{19}$$

$$W_v = \frac{1}{2}W_L + \left(\left(\frac{1}{2}W_L\right)^2 + W_g\right)^{\frac{1}{2}}, \tag{20}$$

$$R = \frac{W_L}{W_v}. \quad (21)$$

Here, W_L and W_g are the full-width of harf maximums originate from pressure and tempature broadening, respectively. Twenty-five wavelengths ($\lambda_c, c = 0 - 14$) listed in Table I were employed for 1628-nm spectrum. For 1654-nm spectrum, one wavelength (λ_c =1653.723 nm) was employed.

Table I Wavelengths used for approximating 1628-nm spectrum

c	λ_c	c	λ_c	c	λ_c	c	λ_c	c	λ_c
0	1627.807	5	1628.046	10	1628.139	15	1628.327	20	1628.568
1	1627.856	6	1628.069	11	1628.154	16	1628.353	21	1628.622
2	1627.925	7	1628.091	12	1628.199	17	1628.508	22	1628.685
3	1628.005	8	1628.100	13	1628.210	18	1628.551	23	1628.700
4	1628.035	9	1628.113	14	1628.279	19	1628.562	24	1628.795

The optimal parameters of (I_c, R, W_v) for the measured conditions of pressure and temperature were determined to minimize the square error

$$E^A = \int \left(A^{approx}(\lambda) - A^{meas}(\lambda)\right)^2 d\lambda. \quad (22)$$

If the parameters of (I_c, R, W_v) were determined for the conditions where the spectra were acquired, they can be determined also for arbitrary condition of 100-760 Torr and 300-773 K with interpolations. As the results, the CH_4 spectrum database can be obtained.

Chapter 4 Design of CT-TDLAS chamber for semiconductor process

4.1 CT-TDLAS measurement system

Figure 9 shows the schematic of the CT-TDLAS measurement system. The LDs and PDs described in Chapter 3 were employed for the light sources and detectors. To scan the wavelengths of the LDs, the applied currents were continuously modulated by saw tooth waveforms with a frequency of 0.5 kHz. The two modulation signals were synchronized but their directions of the current variation were opposite with

each other. The two laser beams were combined by a fiber combiner, and separated into 32 paths by a fiber splitter, then injected into the 32-laser-path cell through collimators. The collimators were placed in four different directions of the cell at 45 degree intervals. The injected laser beams passed through the measured area, and were detected by 32 PDs. The detected signals were stored by a recording system (National Instruments, cRIO-9035) with sampling rate of 500 kHz.

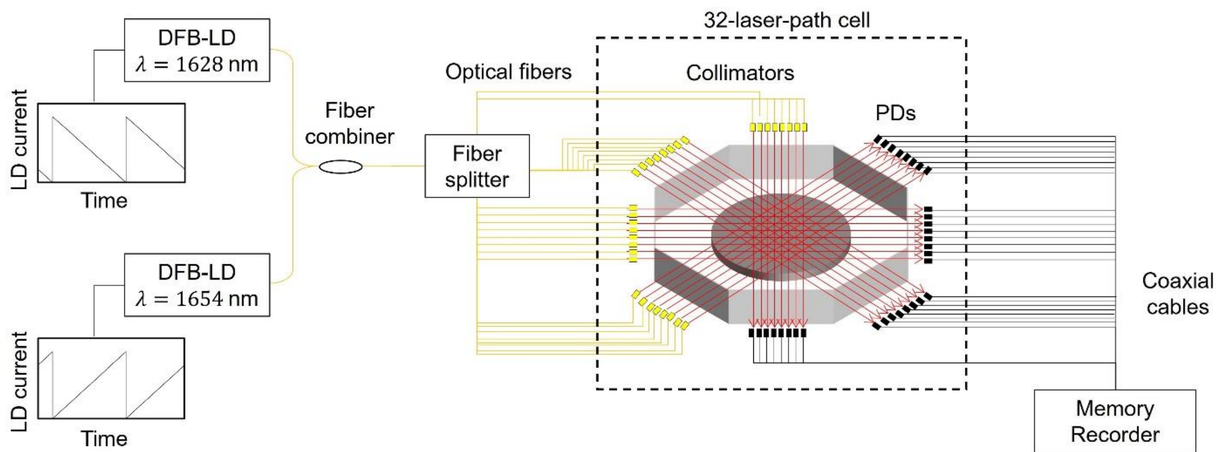

Fig. 9 Schematics of the CT-TDLAS measurement system.

4.2 Chamber structure

We designed a semiconductor chamber that is specialized for our experiments. The top view and cross section of the chamber are shown in Fig. 10. The chamber has five ports on the top of the upper lid. The center port is for attaching a pressure gauge, and the other four are gas inlet ports that are configured with cyclic symmetry on a circle of 60 mm-diameter. Figure 11 shows the 32-laser-path cell installed in the chamber. The cell is sandwiched by upper and lower panels of the chamber via O-rings. The measured area is inside the center circle whose diameter and thickness are 100 mm and 10 mm, respectively. At the bottom of the measured area, a susceptor was places. We prepared for two kinds of susceptor as shown in Figs.12: an aluminum type and a poly-ether-ether-ketone (PEEK) type susceptors. As the temperature of the

aluminum type susceptor can be controlled uniformly, it was used for experiments under a uniform temperature. In the PEEK type susceptor, four aluminum heater blocks whose temperatures are independently controlled are embedded. The centers of the heater blocks were configured on the same circle of 60 mm-diameter. This type of susceptor was used for experiments under an arbitrary temperature distribution. Both susceptors have four exhaust holes, which are located just under the gas inlet ports. The measured area is surrounded by a silica crystal ring (Eikoh Co., Ltd.) whose inner and outer diameters were 100 mm and 107 mm with the tolerance of $\pm$0.05 mm. Thirty-two collimators and PDs are attached around the cell and the 32 laser-paths are intersected in the measured area. The vertical distance between the laser path and the susceptor upper surface is about 1 mm or less. The images of the chamber appearances are shown in Fig. 13.

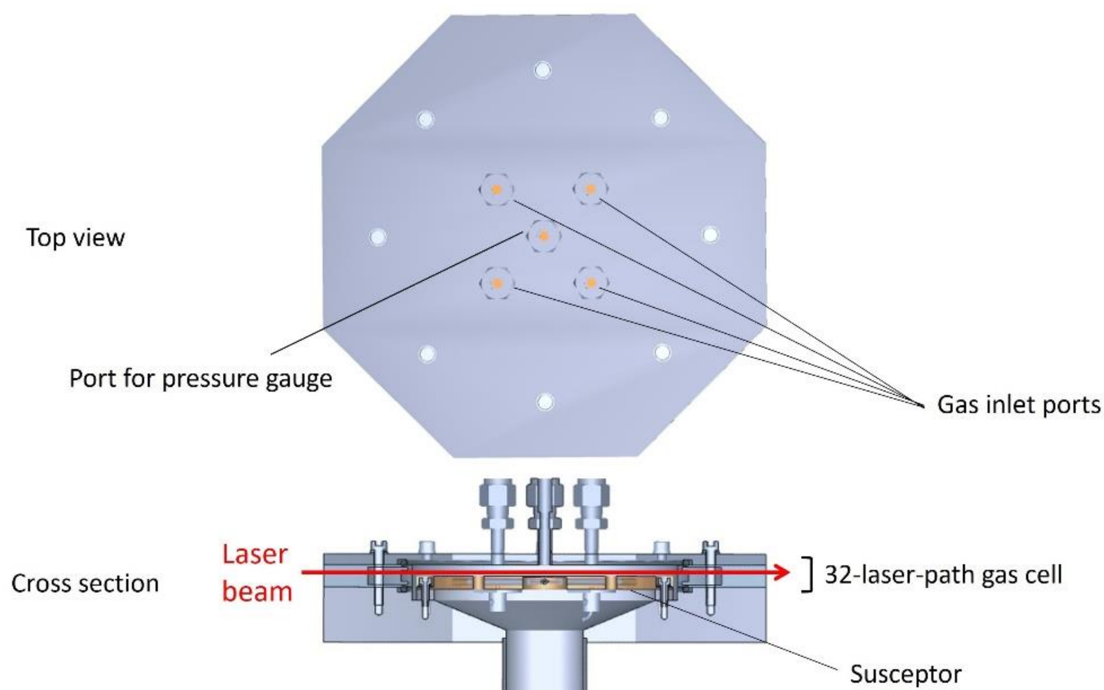

Fig. 10 Structure of the chamber.

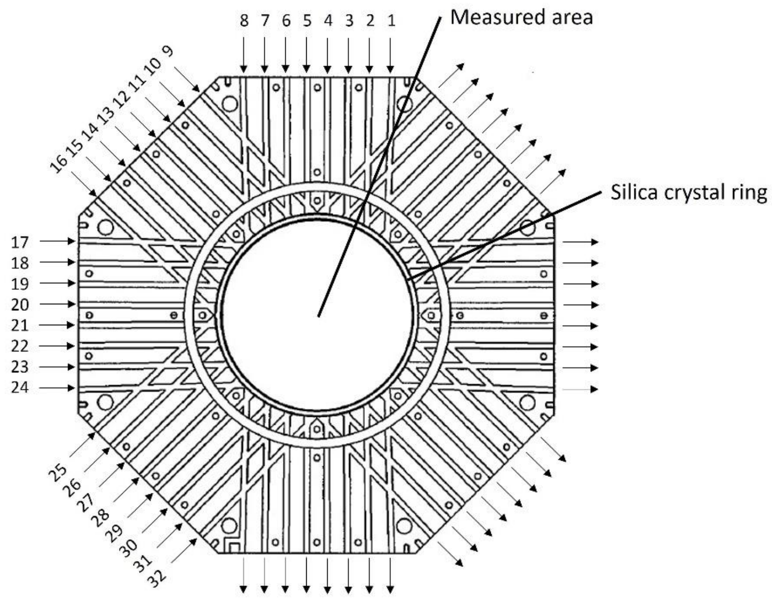

Fig. 11 The 32-lase-path cell. Numbers and arrows indicate path number and laser beam directions, respectively.

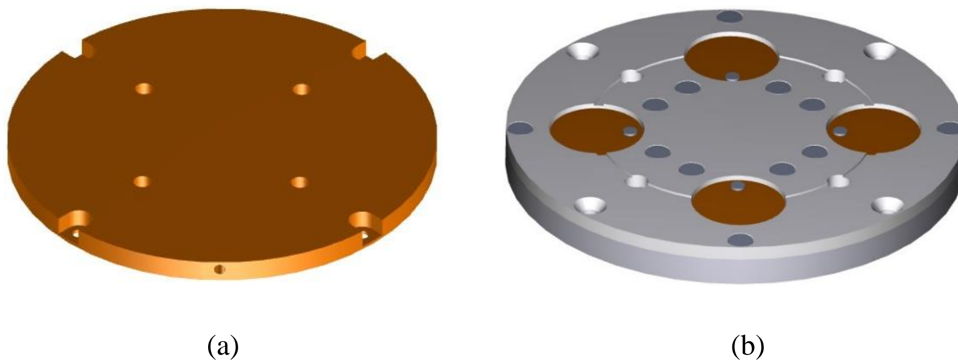

(a) (b)

Fig. 12 (a) An aluminum type susceptor and (b) a PEEK type susceptor.

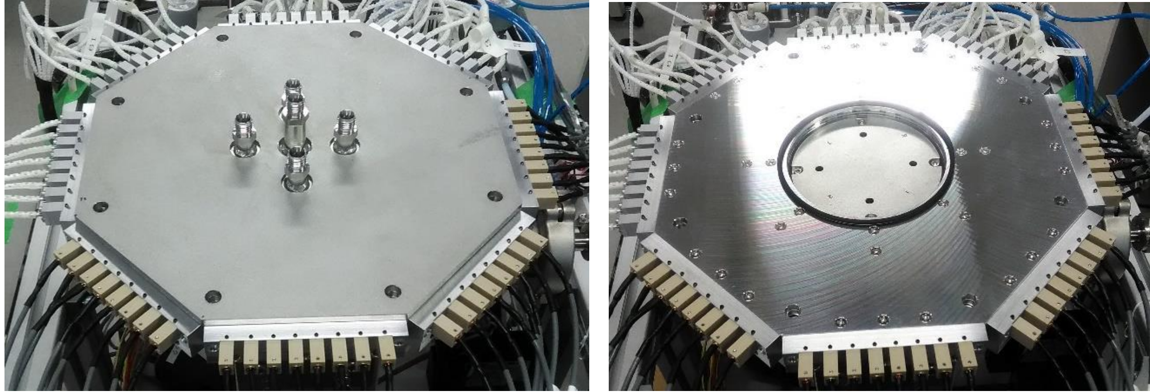

(a) (b)

Fig. 13 Image of the chamber with (a) and without (b) the upper lid.

(The aluminum type susceptor is equipped.)

Chapter 5 Validity checks of CT algorithm

5.1 Validation of concentration distribution algorithm using concentric cylinder

Basic operations of our CT algorithm were checked with a simple experiment using a five-fold concentric cylinder. The structure of the cylinder and the experimental setup are drawn in Fig. 14. The inside of the cylinder was separated into five flow areas by concentric hollow cylinders. The 32-laser-path cell was placed at the upper surface of the cylinder. The diameter of each area was written in Table II.

We measured a CH_4 concentration distribution just above the exit when various concentrations of CH_4 were simultaneously fed into the cylinder. The setting concentrations (Set 1 and Set 2) were listed in Table III. CH_4 was fed from a lower inlet port of each area, and exited through the upper surface of the cylinder to open air. CH_4 flow rate in each area was determined so that the volume passing through unit cross section of each flow area per unit time was all the same. It was expected that CH_4 concentration distribution just

above the exit were almost the same as the distribution of horizontal cross section of the cylinder which were clearly determined by Table III.

The setting and measured with the CT-TDLAS distributions were shown in Fig. 15. The measured distributions reproduced well the setting distributions for both cases. Therefore, it was verified that our CT algorithm basically worked correctly. However the measured distributions showed some blur at boundary of flow areas. The two factors about the blur were considered: (i) mixing of gas concentration after the exit, and (ii) reconstruction limitation due to the available spatial resolution of CT reconstruction. The latter factor was further investigated in the next section.

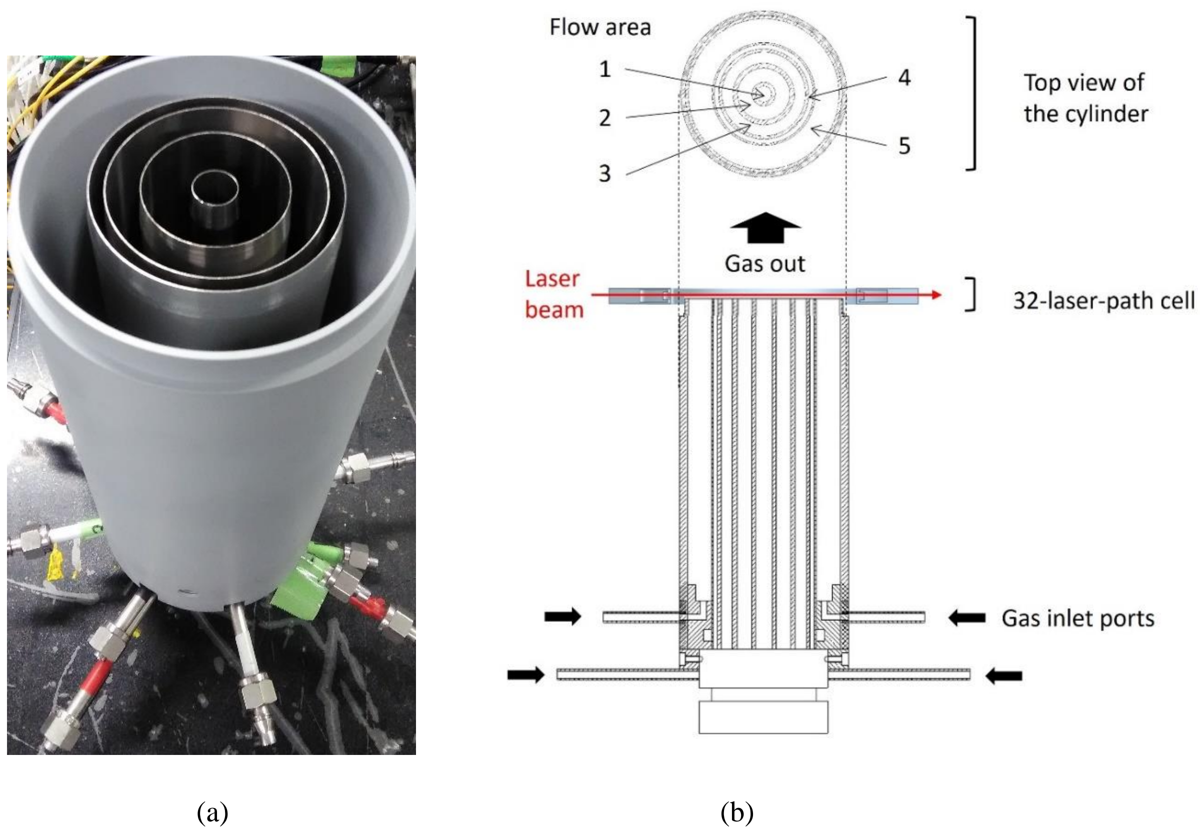

(a) (b)

Fig. 14 Structure of the five-fold concentric cylinder. The image (a) and the experimental setup for the CT algorithm check (b).

Table II Diameter of each flow area.

Flow area	Inner diameter (mm)	Outer diameter (mm)
1	10.3	12.3
2	33.0	39.0
3	53.0	57.0
4	62.6	65.0
5	95.0	99.0

Table III CH_4 concentration fed into each flow area of the five-fold concentric cylinder.

Flow area	CH_4 concentration (%)	
	Set 1	Set 2
1	10	8
2	8	10
3	6	6
4	4	4
5	4	4

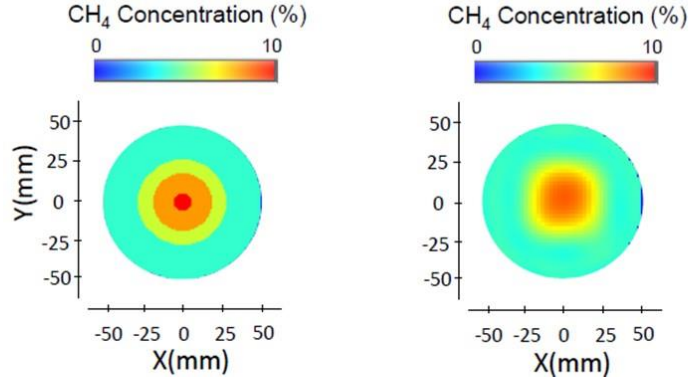

(a) Set 1

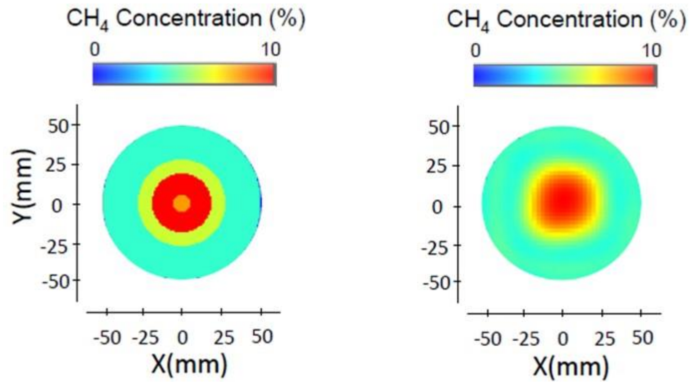

(b) Set 2

Fig. 15 Results of CT algorithm check for Set 1 and Set 2. Setting (left) and measured (right) CH_4 concentration distributions.

5.2 Spatial resolution of reconstructed distribution

The spatial resolution of the CT was defined as the minimum distance where two concentration peaks can be distinguished as clearly defined separate peaks. We assumed two kinds of CH_4 concentration distributions in the measured area of 32-laser-path cell. We calculated 32 spectra under the assumed distributions, and then reconstructed the distribution by the CT calculation based on the 32 spectra. The assumed distributions were isotropic Gaussians which had peak concentration of 10% at the center of the

area, and whose full width at half maximum (FWHM) were 15 mm and 25 mm. The reconstructed results together with the assumed distributions were shown in Fig. 16. The FWHM of CT reconstructed distributions were 22 mm and 34 mm, respectively. In general, it is not avoidable that the CT reconstructed distributions show wider FWHMs than originals and the results were reasonable because the CT calculations are based on absorbance for limited number of paths. However, the FWHM of reconstructed distribution could not be less than 20 mm even when the FWHM of assumed distributions were reduced as less than 15 mm. It means that two peaks placed at a distance within 20 mm could not be distinguished in the CT reconstructed distribution, even if the FWHMs of both peaks were less than 20 mm.

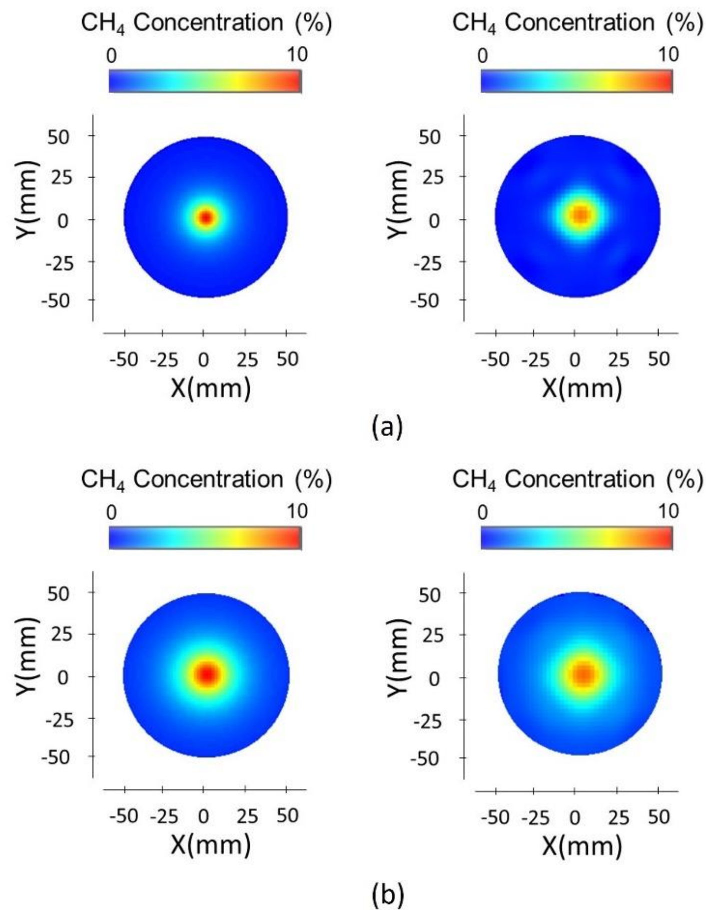

Fig. 16 Results of spatial resolution investigations. Assumed (left) and CT reconstructed (right) CH_4 concentration distributions. The FWHMs of assumed distributions were (a) 15 mm and (b) 25 mm.

5.3 Validation of algorithm for concentration and temperature distributions using computer fluid dynamics

CH_4 concentration and temperature distributions in stable states in the chamber were simulated with the CFD (FloFED, Mentor Graphics). The governing equations for the simulations include the continuous equation, the equation of motion, the energy conservation equation, and the conservation equation of chemical species, which are respectively expressed as follows:

$$\frac{\partial(u_{i_1})}{\partial x_{i_1}} = 0, \tag{23}$$

$$\frac{\partial(\rho u_{i_1})}{\partial t} + \frac{\partial(u_{i_2}\rho u_{i_1})}{\partial x_{i_1}} = -\frac{\partial p}{\partial x_{i_1}} + \frac{\partial}{\partial x_{i_1}}\left(\kappa \frac{\partial u_{i_1}}{\partial x_{i_2}}\right) - \rho g_{i_1}\beta(T - T_0), \tag{24}$$

$$\frac{\partial\left(\rho C_p T\right)}{\partial t} + \frac{\partial(\rho u_{i_1} C_p T)}{\partial x_{i_1}} = \frac{\partial}{\partial x_{i_1}}\left(\lambda \frac{\partial T}{\partial x_{i_1}}\right) + H, \tag{25}$$

$$\frac{\partial\left(Y_{k_1}\right)}{\partial t} + \frac{\partial\left(u_{i_1} Y_{k_1}\right)}{\partial x_{i_1}} = D\frac{\partial^2 Y_{k_1}}{\partial {x_{i_1}}^2}. \tag{26}$$

The equations determine the behavior of ρ (density), u (velocity), p, and T of CH_4. Here, μ is the viscosity coefficient, g is the gravity, β is the thermal expansion coefficient, T_0 is the initial temperature, C_p is the heat capacity, κ is the heat conductivity, H is the enthalpy, D is the diffusion coefficient, and Y_{k_1} is the concentration of gas species k_1 (CH_4 or N_2). Indices $i_1, i_2, i_3 = 1, 2, 3$ correspond to x, y, z components. This simulation was made under the assumption that the inner wall was no-slip and the thermal radiation effect was negligible.

First, we simulated CH_4 concentration distributions in the chamber under uniform susceptor temperature. In this case, distributions in the chamber equipped with the aluminum type susceptor were simulated. The setting concentration fed from each inlet port is listed in Table IV. The configuration of gas inlet ports are illustrated in Fig. 17. The cell pressure, susceptor temperature, and flow rate per unit port were fixed at 760 Torr, 40 °C, and 0.5 slm, respectively. After the simulations, we calculated the 32 spectra

for each simulated distribution. Then, we applied the CT algorithm to check whether the distributions are reconstructed. The simulated and CT reconstructed distributions are shown in Fig. 18. The simulated distributions showed high concentration spots according to the numbers and locations of CH_4 feeding ports. And the CT reconstructed well the original CFD distributions from the calculated 32 path spectra regarding the numbers and locations of high concentration spots.

Table IV Settings for CFD of CH_4 concentration distributions in the chamber. The cell pressure, susceptor temperature, and flow rate per unit port were fixed at 760 Torr, 40 ℃, and 0.5 slm, respectively

Condition	Concentration (%)			
	Port 0	Port 1	Port 2	Port 3
1	10	0	0	0
2	10	0	0	10
3	10	0	10	0
4	10	0	10	10
5	10	0	10	10

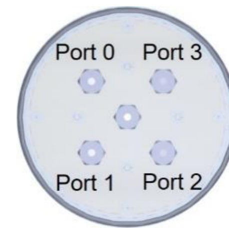

Fig. 17 Configuration of gas inlet ports.

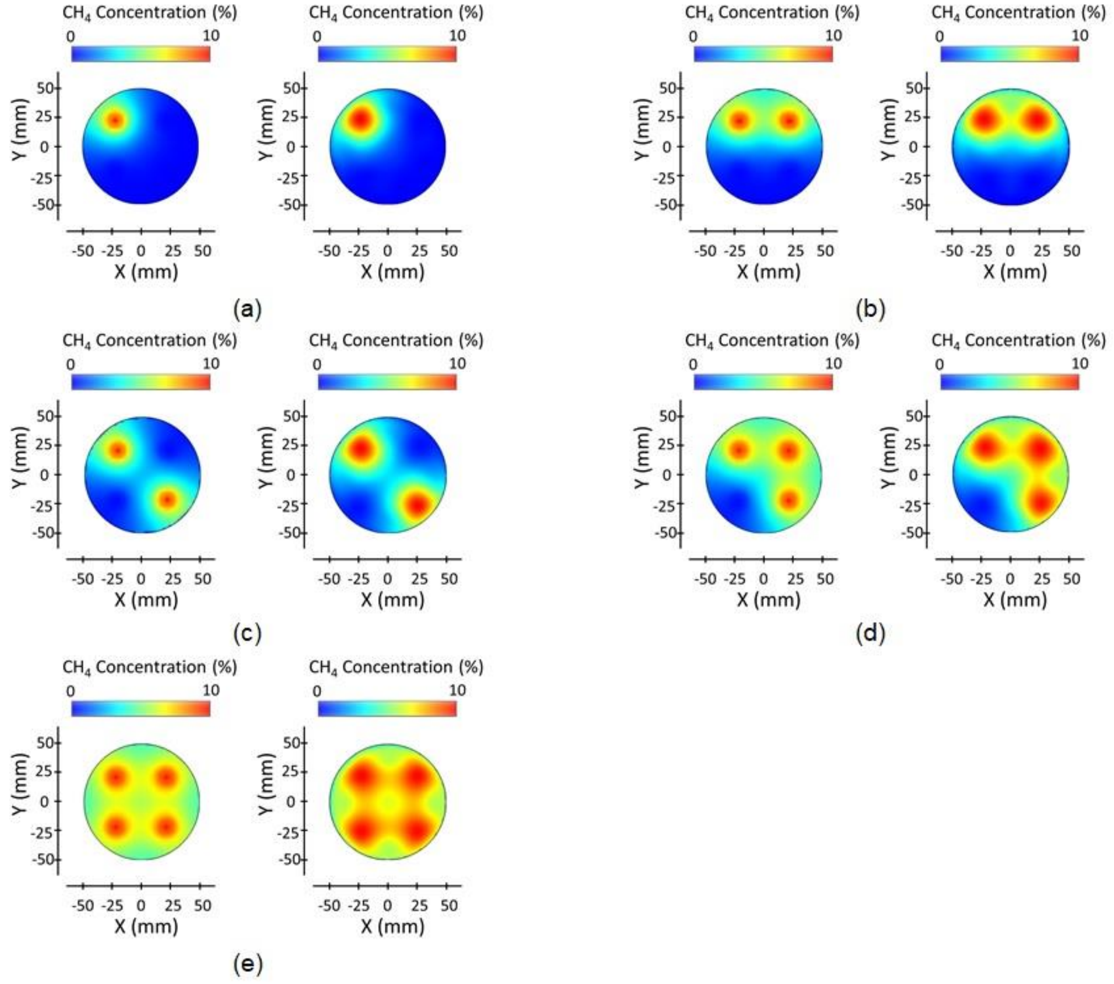

Fig. 18 CFD (left) and CT reconstructed (right) concentration distributions of CH_4 in the chamber. (a)- (e) correspond to the conditions 1-5 listed in Table IV.

To evaluate the differences between the CFD and CT reconstructed distributions quantitatively, the sum of squared differences (SSD) and the zero-mean normalized cross-correlation (ZNCC) on the reference of the CFD distributions were calculated. The SSD is defined as

$$SSD = \frac{1}{X_{max}} \sqrt{\frac{1}{N_1 N_2} \sum_{n_1=0}^{N_1-1} \sum_{n_2=0}^{N_2-1} \left\{ \left(X_{n_1 n_2}\right)_{CFD} - \left(X_{n_1 n_2}\right)_{CT} \right\}^2} . \tag{27}$$

Here $X_{n_1 n_2}$ is the concentration or temperature at each grid, X_{max} is the maximum values in the CFD distribution, N_1 and N_2 are the total numbers of meshes along the x- and y-axis set in the measured area,

respectively. If the SSD is close to "0", the two patterns can be considered as almost the same. The ZNCC is defined as

$$ZNCC = \frac{\sum_{n_1=0}^{N_1-1}\sum_{n_2=0}^{N_2-1}\left\{\left(X_{n_1n_2}-\overline{X}\right)_{CFD}\left(X_{n_1n_2}-\overline{X}\right)_{CT}\right\}}{\sqrt{\sum_{n_1=0}^{N_1-1}\sum_{n_2=0}^{N_2-1}\left(X_{n_1n_2}-\overline{X}\right)_{CFD}^2\sum_{n_1=0}^{N_1-1}\sum_{n_2=0}^{N_2-1}\left(X_{n_1n_2}-\overline{X}\right)_{CT}^2}}, \tag{28}$$

where

$$\overline{X} = \frac{1}{N_1N_2}\sum_{n_1=0}^{N_1-1}\sum_{n_2=0}^{N_2-1}X_{n_1n_2}. \tag{29}$$

If the ZNCC is close to "1", the correlation between the two is high, and they can be considered as almost the same. The calculated SSD and ZNSS values are shown in Table V. For all the distributions, the CT reconstructed distributions spread more widely than the CFD distributions due to the calculations based on limited number of absorbance, as stated in Section 5.2. For that reason, as the number of concentration peaks increased, SSD increased and ZNCC decreased. However, even for the worst cases, SSD of 0.060 and ZNCC of 0.890 were obtained, which were good enough to be considered as almost the same patterns. Therefore, it can be said that the CT reconstructed distributions in the chamber agreed well with the CFD simulated distributions

Table V SSD and ZNCC of concentration distributions for condition 1-5.

Condition	SSD	ZNCC
1	0.013	0.989
2	0.026	0.989
3	0.028	0.973
4	0.043	0.977
5	0.060	0.890

Next, we simulated CH_4 concentration and temperature distributions in the chamber under non-uniform susceptor temperature. In this case, distributions in the chamber equipped with the PEEK type

susceptor were simulated. The conditions used in the simulations are listed in Table VI, where CH_4 concentration of each port was fixed throughout all the conditions and the heater block temperatures were varied. Same as the uniform temperature cases, the distributions were reconstructed with the CT based on the 32 spectra calculated from the simulated distributions. Figure 19 shows the results of the CFD and CT reconstructed CH_4 concentration and temperature distributions. For all conditions, the CFD results show the distributions of high concentrations around the port set at 10% and high temperature spots around the heater blocks set at 125 °C. The CT reconstructed the CFD distributions well though the spatial resolution was not as detailed as that of the CFD.

Table VI Conditions used for CFD simulation for CH_4 concentration and temperature distributions. CH_4 flow rate for each port and temperature of susceptor main body (PEEK) were fixed at 0.2 slm and 25 °C, respectively.

Condition	CH_4 concentration (%)				Heater block temperature (°C)			
	Port 0	Port 1	Port 2	Port 3	Block 0	Block 1	Block 2	Block 3
6					125	25	25	25
7	5	5	5	10	125	125	25	25
8					125	125	125	25
9					125	125	125	125

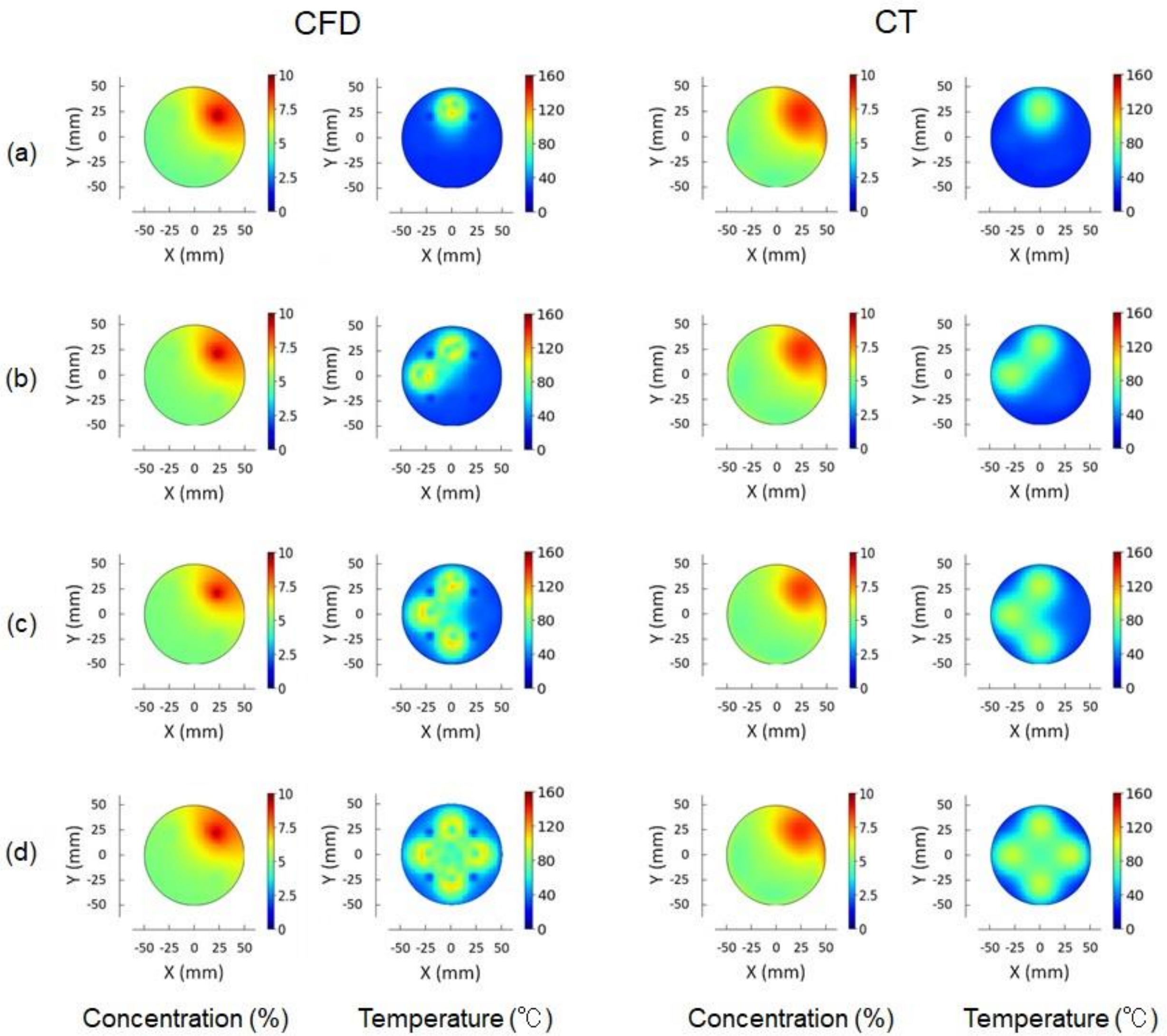

Fig. 19 Comparison of CH_4 concentration and temperature distributions between the CFD (left two columns) and the CT (right two columns).

To simply compare the CFD and CT, we investigated the distributions along x direction at fixed y. Figure 20 exhibits the CFD and CT values of condition 9 versus x plots at $y = 21$ mm ($y = 0$ mm) for concentration (temperature). The CT agreed with the overall trends of the CFD. As discussed in Section 5.2, the minimum spatial resolution of CT reconstructed distribution is 20 mm in the 32-laser-path

configuration. This is why the CT did not follow the peaks and valleys at around $x = \pm 20$ mm in Figs. (a) and around $x = \pm 25$ mm in (b). The resolution of the CT can be improved if the path number increases.

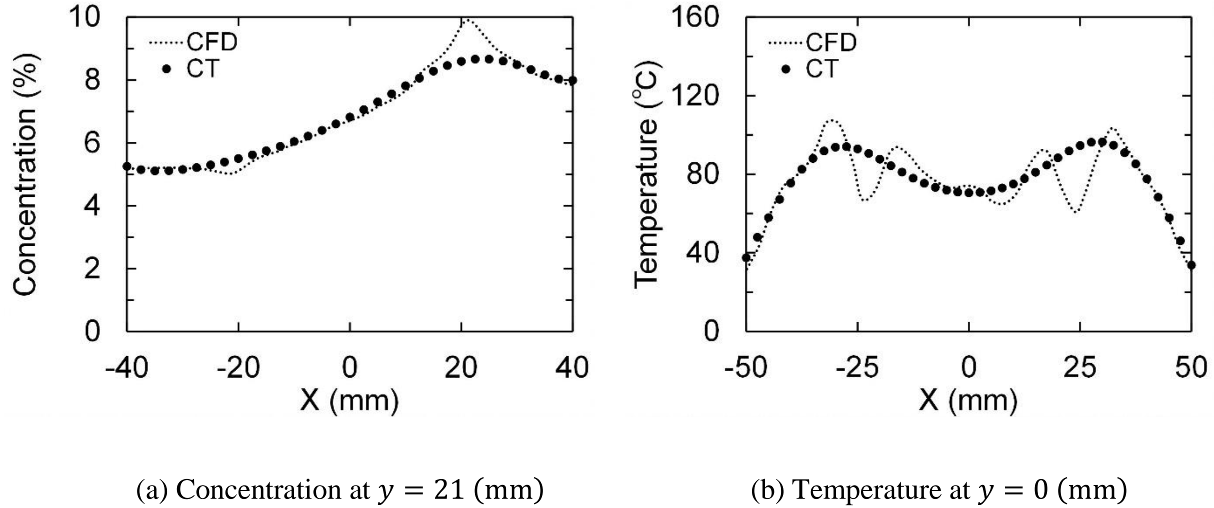

(a) Concentration at $y = 21$ (mm)

(b) Temperature at $y = 0$ (mm)

Fig. 20 CFD and CT values of condition 9 versus $\boldsymbol{x}$ plots.

The calculated SSDs and ZNCCs for condition 6-9 are shown in Table VII. For all conditions, SSDs lower than 0.1 and ZNCCs higher than 0.94 were obtained, which means that the CT reconstructed distributions agreed well with the CFD simulated ones. From these results, it was confirmed that our CT algorithm works well for reconstructing concentration and temperature distributions.

Table VII SSD and ZNCC of concentration and temperature distributions for condition 6-9.

Condition	SSD		ZNCC	
	Concentration	Temperature	Concentration	Temperature
6	0.019	0.037	0.987	0.972
7	0.023	0.058	0.978	0.958
8	0.021	0.060	0.978	0.959
9	0.024	0.067	0.976	0.943

Chapter 6 CT-TDLAS measurements of CH_4 concentration and temperature distributions in chamber

6.1 Experimental system

CH_4 was actually fed into the chamber and the concentration and temperature distributions were measured with the CT-TDLAS. The gas flow system is illustrated in Fig. 21. CH_4 and N_2 were introduced into the chamber, and their flow rates were regulated by mass flow controllers. The pressure in the chamber was regulated by a back pressure regulator. The cables for thermocouples and heaters for regulating the heater blocks passed through an exhaust pipe below the chamber, and were extracted through cable extraction ports in order to seal off the inside the pipe.

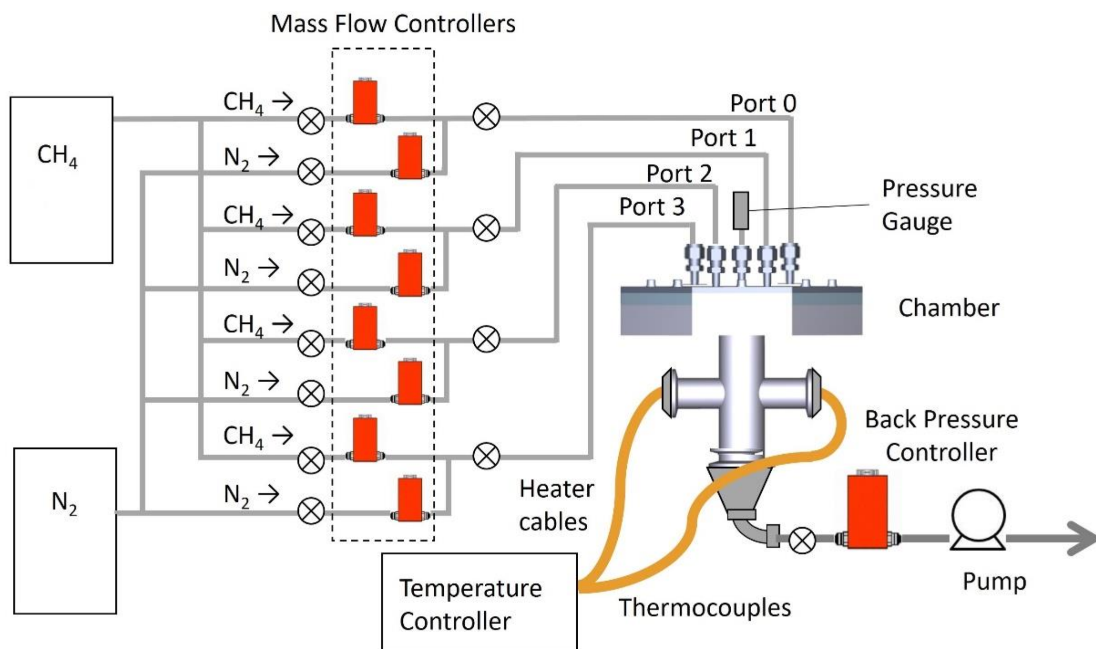

Fig. 21 Gas flow system.

6.2 Concentration distribution measurement

CH_4 concentration distribution in the chamber under a uniform susceptor temperature. The aluminum type susceptor was used in this experiments. We fed CH_4 of 10% from one of four inlet ports and N_2 from the other three ports. Gas flow rate per one inlet port was set at 0.5 slm. Pressure in the chamber and temperature of the susceptor were fixed at 760 Torr and 40 °C, respectively. We performed the experiments four times, changing the location of CH_4 inlet port as shown in Fig. 22.

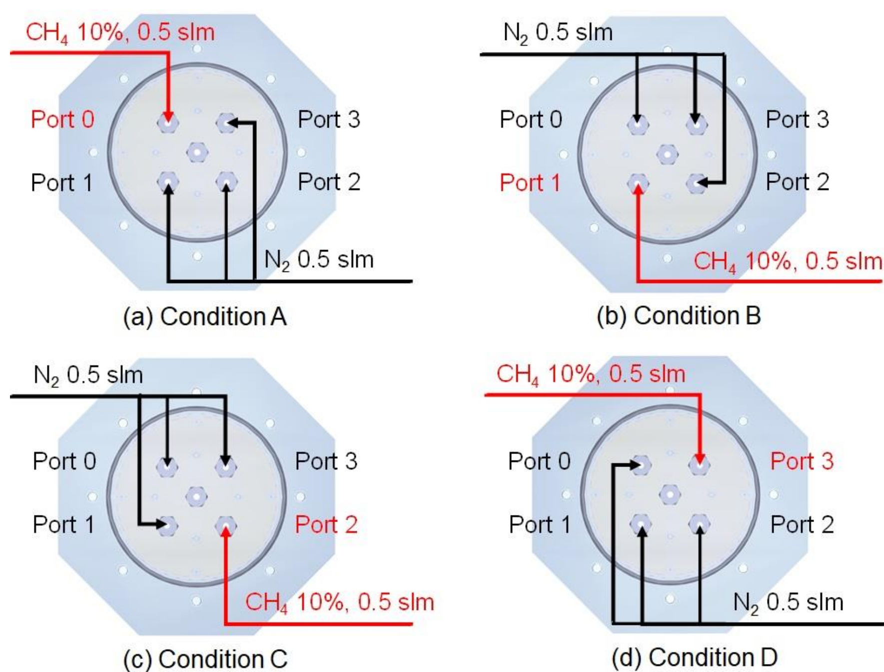

Fig. 22 Conditions of CH_4 concentrations and flow rates for concentration distribution measurements

Figures 23 (a)-(d) show the CH_4 concentration distributions in the chamber measured by the CT-TDLAS. All distributions showed concentration peaks around the location of CH_4 inlet ports. However, the patterns of distributions around the inlet ports were obviously different depending on their location, although all the inlet ports were configured with cyclic symmetry about the center of the chamber and the conditions besides

it were all the same. The concentration close to 10% was widely distributed in Fig. 23 (d). On the other hand, the peak concentration was very low and the concentration hardly spread in (b). These results indicates that the flow impedances of the exhaust holes on the susceptor were different in accordance with their locations; the flow impedance was the lowest at the exhaust hole below port 1, and became higher in the order of 2→0→3. The cause of the difference can be considered that bundles of thermocouple and heater cables passing through the exhaust pipe under the susceptor interrupted the exhaust gas flow as shown in Fig. 24. As the deployment of the cables was not isotropic, the difference of distribution patterns occurred. By the c CT-TDLAS measurements, we could find the unexpected gas flow in the chamber.

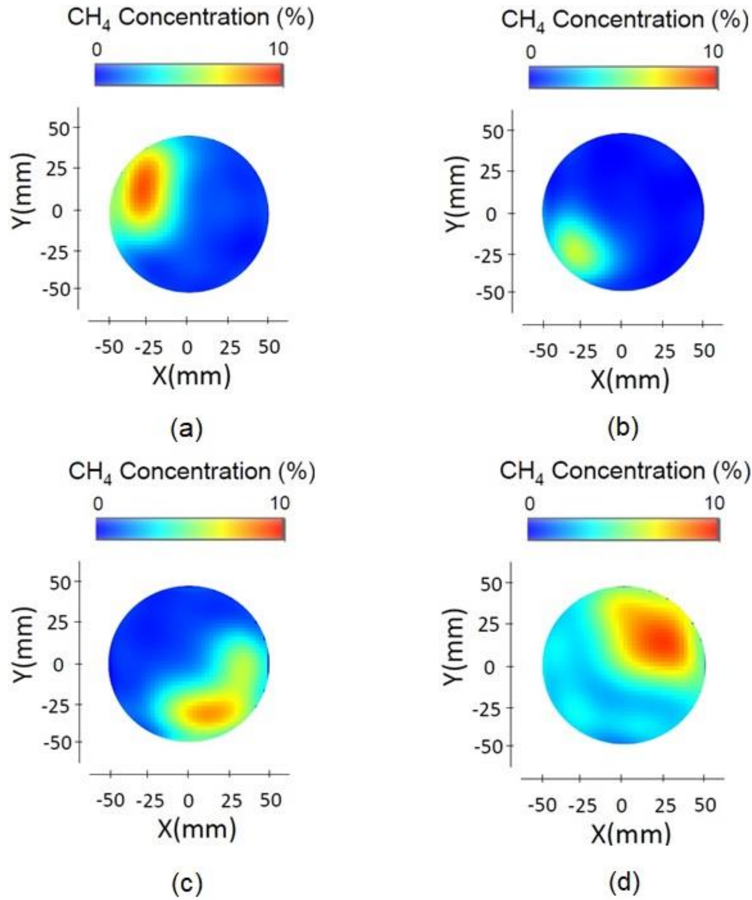

Fig. 23 CH_4 concentration distributions in the chamber measured with the CT-TDLAS.
(a)-(d) correspond to conditions A-D, respectively.

Fig. 24 Backside of the susceptor. The red and yellow cables are thermocouples, and the white cables are heater cables.

6.3 Simultaneous measurement of concentration and temperature distributions

CH_4 concentration and temperature distributions in the chamber were simultaneously measured with the CT-TDLAS. The PEEK type susceptor was used in this experiment. CH_4 was fed into the chamber for various temperature settings of the heater blocks on the susceptor. The feeding CH_4 concentrations were fixed as 10% for one port, and 5% for the other ports. Figure 25 shows the settings of feeding CH_4 concentrations and locations of the heater blocks on the susceptor. The settings of the block temperatures are listed in Table VIII.

Figure 26 shows the measured results. In the concentration distributions of all conditions, high concentrations were observed around the port 3, though overall concentration levels were higher than the CFDs. The reason is considered that the vacuum powers of the exhaust holes were influenced by the flow impedance of the downstream pipe and were weaker than considered in the CFD, as discussed in Section 6.2. In the temperature distributions, high temperature spots around heater blocks set at 125 °C were observed. In condition H, although all heater blocks were set at 125 °C, the measured temperature around the block 3 was higher than temperatures around other blocks. To check the validity of the results, CH_4

temperatures were measured with thermocouples when CH_4 was fed under the same conditions. Four additional thermocouples were introduced on the susceptor through the exhaust holes, and placed on the four heater blocks. The heads of the thermocouples were stood to measure CH_4 temperature directly over the heater blocks. The length of the standing head was 5-7 mm. (In this case, simultaneous CT-TDLAS measurement was not available as the standing heads interrupted the laser beam.) The temperatures measured with thermocouples and the CT-TDLAS together with the setting temperatures are summarized in Fig. 28. The CT-TDLAS values in this figure are temperatures at the center of heater blocks. The measured temperatures do not coincide because the locations were slightly different between the two tests. However, the overall trend of measured temperature distributions agreed well. Especially in condition H, the temperature around heater block 3, which was higher than those of other blocks in the CT-TDLAS measurement, was also higher in the thermocouple measurement. From these results, the validity of the CT-TDLAS measurement was confirmed. The fact that the temperature around one heater block was higher than others means that CH_4 temperature distribution over the susceptor was not completely determined by the temperature settings of the heater blocks. Other factors such as the characteristics of the chamber structure or the gas heat transfer could affect it. Therefore, to regulate the temperature distribution in the chamber, adjusting various parameters based on the measured results of the CT-TDLAS is significantly important. On the other hand, as the concentration distributions in Fig. 26 were almost the same, the variation of the temperature distribution gives almost no impact to the concentration distribution.

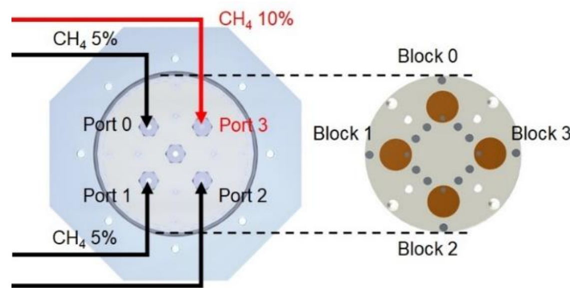

Fig. 25 Settings of CH_4 concentration and locations of the heater blocks on the susceptor.

Table VIII Settings of heater block temperatures

Condition	Temperature (℃)			
	Block 0	Block 1	Block 2	Block 3
E	125	25	25	25
F	125	125	25	25
G	125	125	125	25
H	125	125	125	125

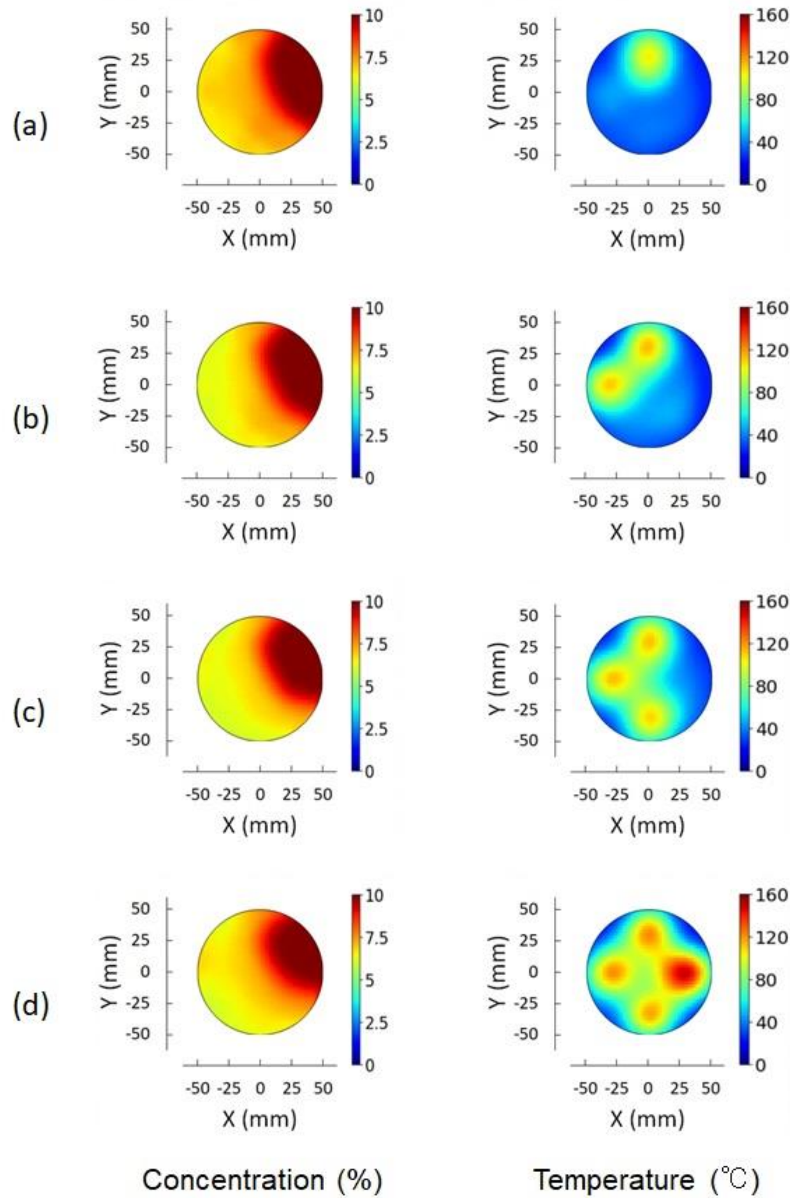

Fig. 26 CH_4 concentration and temperature distributions measured with the CT-TDLAS. (a)-(d) correspond to conditions E-H, respectively.

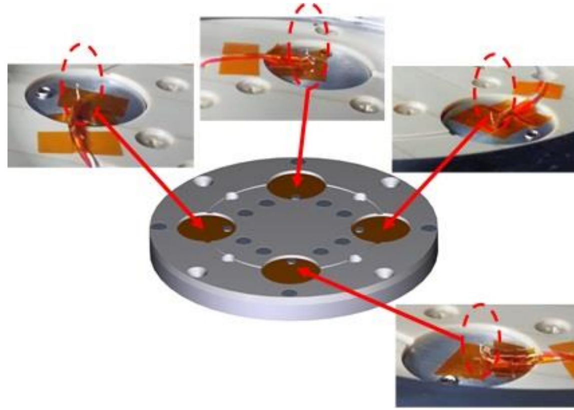

(a)

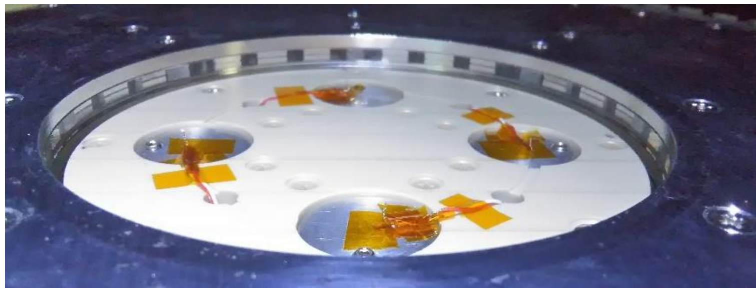

(b)

Fig. 27 Thermocouples set on the heater blocks. (a) Standing thermocouple heads set on heater blocks. (b) Susceptor with thermocouples equipped to the chamber.

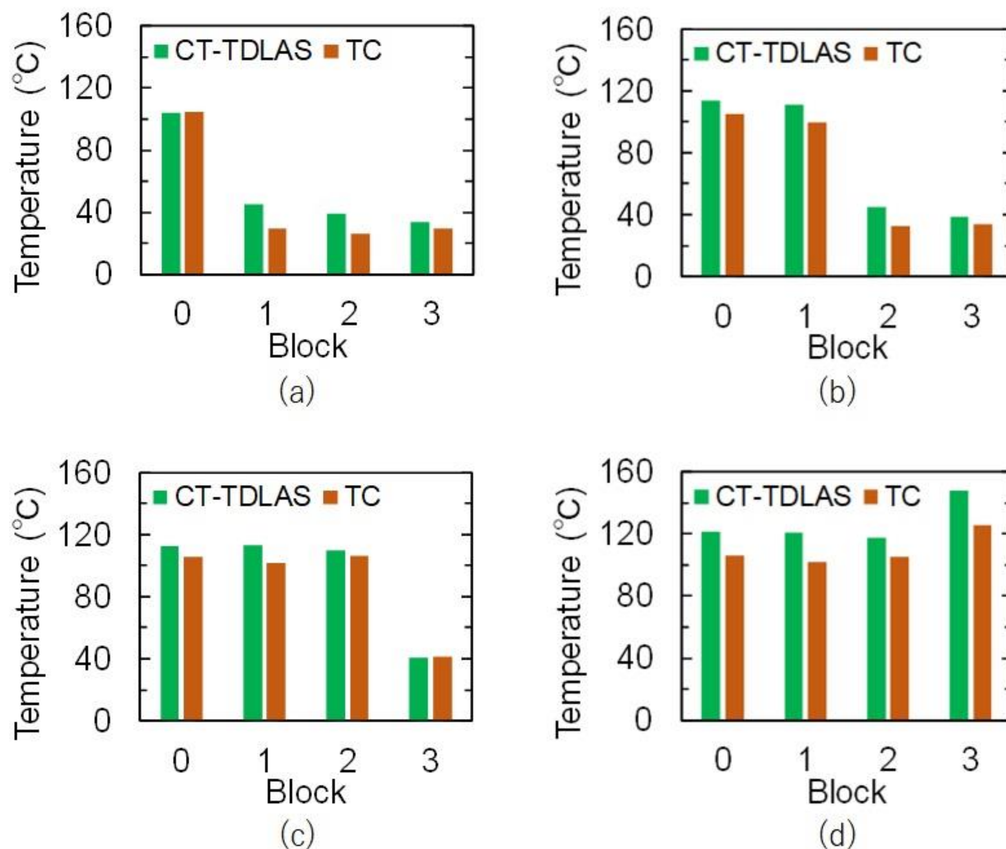

Fig. 28 CH_4 temperatures around heater blocks measured with CT-TDLAS and thermocouples. (a)-(d) correspond to the conditions E-H, respectively.

Chapter 7 Conclusion

In this study, we applied the CT-TDLAS to measure CH_4 concentration and temperature distributions in the semiconductor chamber. After the validity checks of the CT-TDLAS using the five-fold concentric cylinder or the CFD simulations, CH_4 was actually fed into the chamber and the concentration and temperature distributions were measured. In the concertation distribution measurements under a uniform temperature, concentration peaks according to the locations of CH_4 inlet ports were observed. However, the distribution patterns around the inlet ports were obviously different depending on the locations although

the inlet ports were configured with cyclic symmetry. The results indicates the flow impedances of the exhaust holes were different depending on the locations due to the gas flow interruption by bundle of thermocouples and heater cables. In the simultaneous measurements of concentration and temperature distributions, high temperature spots according to the locations of heater blocks set at high temperature were observed. However, the temperatures of the high temperature spots were different depending on the block locations although the temperature settings were all the same. In this way, measured CH_4 concentration and temperature distributions were different from the ones expected from the chamber structure or parameter settings. The results indicates that the CT-TDLAS measurements is indispensable to know actual gas states in the chamber.

Throughout the experiments, the basic performance of the CT-TDLAS measurement for semiconductor process applications was confirmed. Although the conditions of measured gas species and chamber pressure were limited, the CT-TDLAS studied in this work can have some applications for semiconductor process. For example, it can be used for the diagnosis of gas flow or temperature distributions regarding brand-new chambers or chambers under maintenance. We believe the application will certainly contribute the refinements of process. However, to apply the CT-TDLAS to process monitoring of the actual dry etching and improve the CD uniformity described in Chapter 1, some technical hurdles still remains. (1) Most gas species used in the dry etching have absorption peaks in the MIR wavelength region. To measure the gas distributions, the CT-TDLAS system to collect the MIR spectra have to be established. In that case, the parts including a laser source, detectors, and optical fibers have to be changed. (2) The dry etchings are generally implemented at less than 1 Pa. To collect absorption spectra in such low pressure conditions, the sensitivity improvement of the CT-TDLAS system are required. (3) To control the dry etching based on the CT-TDLAS measured distributions, fast processing determining the distributions for one second or less is necessary, although the current CT algorithm takes several seconds.

If these technical hurdles are overcome, the application window of the CT-TDLAS for semiconductor process can be largely broaden. These tasks are left to our future work.

References

[1] T. Tanaka, M. Kido, K. Yahashi, M. Oomura, R. Tatsumata, M. Kito, Y. Fukumizu, S. Sato, Y. Nagata, Y. Matsuoka, Y. Iwata, H. Aochi, and A. Nitayama, "Bit Cost Scalable Technology with Punch and Plug Process for Ultra High Density Flash Memory," *Proc. Symp. VLSI Technol.,* p. 14, 2007.

[2] H. Kawasaki, V. S. Basker, T. Yamashita, C.-H. Lin, Y. Zhu, J. Faltermeier, S. Schmitz, J. Cummings, S. Kanakasabapathy, and H. Adhikari, et al., "Challenges and solutions of FinFET integration in an SRAM cell and a logic circuit for 22 nm node and beyond," *Proc. Int. Electron Devices Meet.,* p. 289, 2009.

[3] V. S. Basker, T. Standaert, H. Kawasaki, C. -C. Yeh, K. Maitra, T. Yamashita, J. Faltermeier, H. Adhikari, H. Jagannathan, J. Wang, H. Sunamura, S. Kanakasabapathy, S. Schmitz, J. Cummings, A. Inada, C. -H. Lin, P. Kulkarni, Y. Zhu, and J. Kuss, et al., "A 0.063 μm2 FinFET SRAM cell demonstration with conventional lithography using a novel integration scheme with aggressively scaled fin and gate pitch," *Proc. Symp. VLSI Technol.,* p. 11488252, 2010.

[4] T. Yamashita, V.S. Basker, T. Standaert, C-C Yeh, J. Faltermeier, T. Yamamoto , C-H Lin, A. Bryant, K. Maitra , P. Kulkarni, S. Kanakasabapathy, H. Sunamura, J. Wang, H. Jagannathan, A. Inada, J. Cho, R. Miller, B. Dori, V. Paruchuri, and H. Bu, et al., *ECS Transactions,* vol. 34, p. 81, 2011.

[5] T. Tatsumi, "Plasma control technologies on semiconductor device fabrications," *Oyobutsuri,* vol. 85, p. 761, 2016, in Japanese.

[6] K. Ishikawa, T. Ishijima, T. Shiraguji, S. Armini, E. Despiau-Pujo, R. A. Gattscho, K. J. Kanarik, G. J. Leusink, N. Marchack, T. Murayama, Y. Morikawa, G. S. Oehrin, S. Park, H. Hayashi, and K. Kinoshita, "Rethinking surface reactions in nanoscale dry process toward atomic precision and beyond: a physics and chemistry perspective," *Jpn. J. Appl. Phys.,* vol. 58, p. SE0801, 2019.

[7] K. J. Kanarik, T. Lill, E. A. Hudson, S. Sriraman, S. Tan, J. Marks, V. Vahedi, and R. A. Gottscho, "Overview of atomic layer etching in the semiconductor industry," *J. Vac. Sci. Technol. A,* vol. 33, p. 020802, 2015.

[8] M. J. Cooke, "Impact of Atomic Layer Etching on Process Tool Design," *J. Solid State Sci. Technol.,* vol. 4, p. N5001, 2015.

[9] C. T. Carver, J. J. Plombon, P. E. Romero, S. Suri, T. A. Tronic, and R. B. Turkot, "Atomic Layer Etching: An Inductry Perspective," *J. Solid State Sci. Technol.,* vol. 4, p. N5005, 2015.

[10] S. Tan, W. Yang, J. Kanarik, T. Lill, V. Vahedi, J. Marks, and R. A. Gottscho, "Highly Selective Directional Atomic Layer Etching of Sillicon," *J. Solid State Sci. Technol.,* vol. 4, p. N5010, 2015.

[11] G. S. Oehrlein, D. Metzler, and C. Li, "Atomic Layer Etching at the Tipping Point: An Overview," *J. Solid State Sci. Technol.,* vol. 4, p. N5041, 2015.

[12] S. U. Engelmann, R. L. Bruce, M. Nakamura, D. Metzler, S. G. Walton, and E. A. Joseph, "Challenges of tailoring surface chemistry and plasma/surface interactions to advance atomic layer etching," *J. Solid State Sci. Technol.,* vol. 4, p. N0554, 2015.

[13] P. L. G. Ventzek, S. D. Sherpa, M. Wang, V. Rastogi, and A. Ranjan, "Control of Atomic Layer Reactions in Plasma Processing," *ECS Trans.,* vol. 75, p. 25, 2016.

[14] M. Honda, "Atomic layer etching using plasma (ALE)," *Oyobutsuri,* vol. 88, p. 173, 2019, in Japanese.

[15] R. W. Johnson, A. Hultqvist, and S. F. Bent, "A brief review of atomic layer deposition: from fundamentals to applications," *materialstoday,* vol. 17, p. 236, 2014.

[16] S. Tachi, M. Izawa, K. Tsujimoto, T. Kure, N. Kofuji, and K. Suzuki, "Near-surface interactions and their etching-reaction model in metal plasma-assisted etching," *J. Vac. Sci. Technol. A,* vol. 16, p. 250, 1998.

[17] S. Hwang and K. Kanarik, "Evolution of across-wafer uniformity control in plasma etch," *Solid State Technol.,* vol. 59, p. 16, 2016.

[18] C. G. N. Lee, K. J. Kanarik, and R. A. Gottscho, "The grand challenges of plasma etching: manufacturing perspective," *J. Phys. D: Appl. Phys.,* vol. 47, p. 273001, 2014.

[19] K. Ishikawa, K. Karahashi, T. Ishijima, S. I. Cho, S. Elliott, D. Hausmann, D. Mocuta, A. Wilson, and K. Kinoshita, "Progress in nanoscale dry processes for fabrication of high-aspect-ratio features: How can we control critical dimension uniformity at the bottom?," *Jpn. J. Appl. Phys.,* vol. 57, p. 06JA01, 2018.

[20] A. P. Milenin, W. Boullart, F. Quli, and Y. Wen, "Study on processing step uniformity tuning during FET fabrication and sensor wafer response as a function of chuck temperature adjustment," *Jpn. J. Appl. Phys.,* vol. 53, p. 03DC02, 2014.

[21] T. Lill, S. Tan, K. J. Kanarik, Y. Kimura, G. Kamarthy, M. Shen, V. Vahedi, J. Marks, and R. A. Gottscho, "Patterning in the Era of Atomic Scale Fidelity," *Proc. SPIE,* vol. 9428, p. 942809, 2015.

[22] F. Fang, A. Vaid, A. Vinslava, R. Casselberry, S. Mishra, D. Dixit, P. Timoney, D. Chu, C. Porter, D. Song, Z. Ren, "Correction study of actual temperautre profile and in-line metrology measurements for within-wafer uniformity improvement and wafer edgge yield enhancement," *Proc. SPIE,* vol. 10585, p. 105851Q, 2018.

[23] A. U. Haq, D. Djurdjanovic, "Virtual metrology concept for predicting defect levels in semiconductor manufacturing," *Procedia CIRP,* vol. 57, p. 580, 2016.

[24] K. Nomura, T. Okazaki, S. Yasuda, A. Kawashima, H. Tani, and K. Matsuda, "Virtual metrology of dry etching process characteristics using EES and OES," *Proc. AEC/APC Symp. Asia,* pp. PC-O-018, 2011.

[25] M. Ito, H. Hamaoka, R. Veerasingam, S. K. Nam, E. Sevillano,and K. Nojiri, "TEOS etch rate predictions using virtual metrology," *Proc. Int. Symp. Dry Process,* p. 33, 2012.

[26] S. Yasuda, T. Okazaki, and K. Nomura, "The VM·APC activities in Sony Semiconductor," *Proc. AEC/APC Symp. Asia,* pp. PC-O-22, 2013.

[27] T. Lill, K. J. Kanarik, S. Tan, S. Berry, A. Fischer, V. Vahedi, and R. A. Gottscho, "Atomic Layer Etching: Benefits and Challenges," *Proc. EDTM,* p. 41, 2018.

[28] T. Lill, S. Tan, K. J. Kanarik, Y. Kimura, G. Kamarthy, M. Shen, V. Vahedi, J. Marks, and R. A. Gottscho, "Patterning in the era of atomic scale fidelity," *Proc. SPIR,* vol. 9428, p. 942809, 2015.

[29] P. L. G. Ventzek, S. D. Sherpa, M. Wang, V. Rastogi, and A. Ranjan, "Control of Atomic Layer Reactions in Plasma Processing," *ECS Transactions,* vol. 75, p. 25, 2016.

[30] A. Ranjan, M. Wang, S. D. Sherpa, and V. Rastogi, "Implementation of atomic layer etching of silicon: Scaling parameters, feasibility, and profile control," *J. Vac. Sci. Technol. A,* vol. 34, p. 31304, 2016.

[31] C. M. Huard, S. J. Lanham, and M. J. Kushner, "Consequences of atomic layer etching on wafer scale uniformity in inductively coupled plasmas," *J. Phys. D: Appl. Phys,* vol. 51, p. 155201, 2018.

[32] K. J. Kanarik , S. Tan and R. A. Gottscho, "Atomic Layer Etching: Rethinking the Art of Etch," *J. Phys. Chem. Lett.,* vol. 9, p. 4814, 2018.

[33] T. W. Kim and E. S. Aydil, "Effects of Chamber Wall Conditions on Cl Concentration and Si Etch Rate Uniformity in Plasma Etching Reactors," *J. Electrochem. Soc.,* vol. 150, p. G418, 2003.

[34] M. Fukasawa, A. Kawashima, N. Kuboi, H. Takagi, Y. Tanaka, H. Sakayori, K. Oshima, K. Nagaharta, and T. Tatsumi, "Prediction of fluctuations in plasma wall interactions using an EES," *Proc. Dry Process Int. Symp.,* p. 247, 2008.

[35] N. Kuboi, M. Fukasawa, and T. Tatsumi, "Advanced simulation technology for etching process desing for CMOS device applications," *Jpn. J. Appl. Phys.,* vol. 55, p. 07LA02, 2016.

[36] W. Zeller, L. Naehle, P. Fuchs, F. Gerschuetz, L. Hildebrandt, and J. Koeth, "DFB Lasers Between 760 nm and 16 µm for Sensing Applications," *Sensors,* vol. 10, p. 2492, 2010.

[37] M.A. Bolshov, Yu. A. Kuritsyn, and Yu. V. Romanovskii, "Tunable diode laser spectroscopy as a technique for combustion diagnostics," *Spectrochimica Acta B,* vol. 106, p. 45, 2015.

[38] Q. He, C. Zheng, H. Liu, B. Li, Y. Wang, and F. K. Tittel, "A near-infrared acetylene detection system based on a 1.534 µm tunable diode laser and a miniature gas chamber," *Infrared Phys. and Tech.,* vol. 93, p. 75, 2016.

[39] P. Kluczynski, J. Jahjah, L. Nahle, O. Axner, S. Belahsene, M. Fischer, J. Koeth, Y. Rouillard, J. Westberg, A. Vicet, and S. Lundqvist, "Detection of acetylene impurities in ethylene and polyethylene manufacturing processes using tunable diode laser spectroscopy in the 3-µm range," *Appl. Phys. B,* vol. 105, p. 427, 2011.

[40] C. Li, L. Dong, C. Zheng, and F. K. Tittel, "Compact TDLAS based optical sensor for ppb-level ethane detection by use of a 3.34 µm room-temperature CW interband cascade laser," *Sens. And Actuators B,* vol. 232, p. 188, 2016.

[41] L. Dong, F. K. Tittel, C. Li, N. P. Sanchez, H. Wu, C. Zheng, Y. Yu, A. Sampaolo, and R. J. Griffin, "Compact TDLAS based sensor design using interband cascade lasers for mid-IR trace gas sensing," *Opt. Exp. ,* vol. 24, p. A528, 2016.

[42] W. Ye, C. Li, C. Zheng, N. P. Sanchez, A. K. Gluszek, A. J. Hudzikowski, L. Dong, R. J. Griffin, and F. K. Tittel, "Mid-infrared dual-gas sensor for simultaneous detection of methane and ethane using a single continuous-wave interband cascade laser," *Opt. Exp. ,* vol. 24, p. 16973, 2016.

[43] C. Zheng, W. Ye, N. P. Sanchez, C. Li, L. Dong, Y. Wang, R. J. Griffin, F. K. Tittel, "Development and field deployment of a mid-infrared methane sensor without pressure control using interband cascade laser absorption spectroscopy," *Sens. And Actuators B,* vol. 244, p. 365, 2016.

[44] C. Li, C. Zheng, L. Dong, W. Ye, F. K. Tittel, Y. Wang, "Ppb-level mid-infrared ethane detection based on three measurement schemes using a 3.34-µm continuous-wave interband cascade laser," *Appl. Phys. B,* vol. 122, p. 185, 2016.

[45] A. A. Kosterev, R. F. Curl, F. K. Tittel, M. Rochat, M. Beck, D. Hofstetter,, "Chemical sensing with pulsed QC-DFB lasers operating at 15.6 µm," *Appl. Phys. B,* vol. 351, p. B75, 2002.

[46] R. F. Curl, F. Capasso, C. Gmachl, A. A. Kosterev, B. McManus, R. Lewicki, M. Pusharsky, G. Wysocki, and F. K. Tittel,, "Quantum cascade lasers in chemical physics," *Chem. Phys. Lett.,* vol. 1, p. 487, 2010.

[47] M. S. Vitiello, G. Scalari, B. Williams, and P. D. Natale, "Quantum cascade lasers: 20 years of challenges," *Opt. Exp. ,* vol. 5167, p. 23, 2015.

[48] D. Hayashi, Y. Sato, M. Minami, N. Muramatsu, and M. Iwaya, "Cp2Mg in-situ monitoring in a MOVPE reactor using a quantum cascade laser," *Jpn. J. Appl. Phys.,* vol. 58, p. SC1013, 2019.

[49] M. Hubner, D. Marinov, O. Guaitella, A. Rousseau, and J. Ropcke, "On time resolved gas temperature measurements in a pulsed dc plasma using quantum cascade laser absorption spectroscopy," *Meas. Sci. and Technol.,* vol. 23, p. 115602, 2012.

[50] J. Ropcke, S. Welzel, N. Lang, F. Hempel, L. Gatilova, O. Guaitella, A. Rousseau, and P.B. Davies, "Diagnostic studies of molecular plasmas using mid-infrared semiconductor lasers," *Appl. Phys. B,* vol. 92, p. 335, 2008.

[51] J. Ropcke, P. B. Davies, S. Hamann, M. Hannemann, N. Lang, and H. van Hleden, "Applying Quantum Cascade Laser Spectroscopy in Plasma Diagnostics," *photonics,* vol. 3, p. 45, 2016.

[52] N. Lang, S. Zimmermann, H. Zimmermann, U. Macherius, B. Uhlig, M. Schaller, S. E. Schults, and J Ropke, "On treatment of ultra-low-k SiCOH in CF4 plasmas: correlation between the concentration of etching products and etching rate," *Appl. Phys. B,* vol. 119, p. 219, 2015.

[53] M. Hubner, N. Lang, S. Zimmermann, S. E. Schlz, W. Buchholtz, J. Ropcke, and J. H. van Helden, "Quantum cascade laser based monitoring of CF2 radical concentration as a diagnostic tool of dielectric etching plasma processes," *Appl. Phys. Lett. ,* vol. 106, p. 031102, 2015.

[54] M. Hori, H. Kondo, and M. Hiramatsu, "Radical-controlled plasma processing for nanofabrication," *J. Phys. D: Appl. Phys.,* vol. 44, p. 174027, 2011.

[55] V. L. Kasyutich, and P. A. Martin, "Towards a two-dimensional concentration and temperature laser absorption tomography sensor system," *Appl. Phys. B,* vol. 102, p. 149, 2011.

[56] L. Ma and W. Cai, "Numerical investigation of hyperspectral tomography for simultaneous temperature and concentration imaging," *Appl. Opt. ,* vol. 47, p. 3751, 2008.

[57] F. Wang, K. F. Cen, N. Li, J. B. Jeffries, Q. X. Huang, J. H. Yan, and Y. Chi, "Two-dimensional tomography for gas concentration and temperature distributions based on tunable diode laser absorption spectroscopy," *Meas. Sci. Tech. ,* vol. 21, p. 045301, 2010.

[58] W. Cai, and C.F. Kaminski, "A numerical investigation of high-resolution multispectral absorption tomography for flow thermometry," *Appl. Phys. B,* vol. 119, p. 29, 2015.

[59] S. J. Grauer, J. Emmert , S. T. Sanders, S. Wagner and K. J. Daun, "Multiparameter gas sensing with linear hyperspectral absorption tomography," *Meas. Sci. Technol.,* vol. 30, p. 105401, 2019.

[60] P. Wright, C. A. Garcia-Stewart, S. J. Carey, F. P. Hindle, S. H. Pegrum, S. M. Colbourne, P. J. Turner, W. J. Hurr, T. J. Litt, S. C. Murray, S. D. Crossley, K. B. Ozanyan, and H. McCann , "Toward in-cylinder absorption tomography in a production engine," *Appl. Opt. ,* vol. 44, p. 6578, 2005.

[61] P. Wright, N. Terzija, J. L. Davidson, S. Garcia-Castillo, C. Garcia-Stewart, S. Pegrum, S. Colbourne, P. Turne, S. D. Crossley, T. Litt, S. Murray, K. B. Ozanyan, H. McCann, "High-speed chemical species tomography in a multi-cylinder automotive engine," *Chem. Eng. J. ,* vol. 158, p. 2, 2010.

[62] X. An, T. Kraetschmer, K. Takami, S. T. Sanders, L. Ma, W. Cai, X. Li, S. Roy and J. R. Gord, "Validation of temperature imaging by H2O absorption spectroscopy using hyperspectral tomography in controlled experiments," *App. Opt.,* vol. 50, p. A29, 2011.

[63] C. Liu, L. Xu, Z. Cao and H. McCann, "Reconstruction of Axisymmetric Temperature and Gas Concentration Distributions by Combining Fan-Beam TDLAS With Onion-Peeling Deconvolution," *IEEE Trans. Instr. Meas.,* vol. 63, p. 3067, 2014.

[64] W. Cai, and C. F. Kaminski, "A tomographic technique for the simultaneous imaging of temperature, chemical species, and pressure in reactive flows using absorption spectroscopy with frequency-agile lasers," *App. Phys. Lett.,* vol. 104, p. 034101, 2014.

[65] W. Cai, and C. F. Kaminski, "Multiplexed absorption tomography with calibration-free wavelength modulation spectroscopy," *App. Phys. Lett.,* vol. 104, p. 154106, 2014.

[66] Z. Wang, W Zhou, T. Kamimoto, Y. Deguchi, J. Yan, S. Yao, K. Girase, M. Jeon, Y. Kidoguchi, Y. Nada , "Two-Dimensional Temperature Measurement in a High-Temperature and High-Pressure Combustor Using Computed Tomography Tunable Diode Laser Absorption Spectroscopy (CT-TDLAS) with a Wide-Scanning Laser at 1335–1375 nm," *Appl. Spect. ,* vol. 4, 2019.

[67] T. Kamimoto and Y. Deguchi, "2D Temperature Detection Characteristics of Engine Exhaust Gases UsingCT Tunable Diode Laser Absorption Spectroscopy," *Int. J. Mech. Syst. Eng.,* vol. 1, p. 109, 2015.

[68] H. Matsui, K. Udagawa, Y. Deguchi and T. Kamimoto, "Simultaneous two cross-sectional measurements of NH3 concentration in bent pipe flow using CT-tunable diode laser absorption spectroscopy," *J. Therm. Sci. Tech.,* vol. 14, p. JTST0016, 2019.

[69] L. Ma, X. Li, S. T. Sanders, A. W. Caswell, S. Roy, D. H. Plemmons, and J. R. Gord, "50-kHz-rate 2D imaging of temperature and H2O concentration at the exhaust plane of a J85 engine using hyperspectral tomography," *Opt. Exp. ,* vol. 21, p. 1152, 2013.

[70] J. Wang, Y. Song, Z. Li, A. Kempf and A. He , "Multi-directional 3D flame chemiluminescence tomography based on lens imaging," *Opt. Lett.,* vol. 40, p. 1231, 2015.

[71] T. Yu, H. Liu and W. Cai, "On the quantification of spatial resolution for three-dimensional computed tomography of chemiluminescence," *Opt. Exp.* , vol. 25, p. 24093, 2017.

[72] M. Jeon M, D. Doh, Y. Deguchi, T. Kamimoto and M. Cui, "Evaluation of 3D measurement using CT-TDLAS," *Mod. Phys. Lett. B,* vol. 33, p. 1940018, 2019.

[73] D. Hayashi, J. Nakai, M. Minami, K. Fujita, T. Kamimoto, and Y. Deguchi, "CH4 Concentration Distribution in a Semiconductor Process Chamber Measured by the CT-TDLAS," *J. Solid State Sci. Technol.,* vol. 7, p. Q218, 2018.

[74] D. Hayashi, J. Nakai, M. Minami, T. Kamimoto, and Y. Deguchi, "Simultaneous measurement of CH4 concentration and temperature distributions in a semiconductor process chamber," *J. Phys. D: Appl. Phys.,* vol. 52, p. 485107, 2019.

[75] M. Lackner, "Tunable diode laser absorption spectroscopy (TDLAS) in the process industries- a review," *Rev. Chem. Eng.,* vol. 23, p. 65, 2007.

[76] Y. Deguchi, T. Kamimoto, Z. Z. Wang, J. J. Yang, J. P. Liu, H. Watanabe, R. Kurose, "Applications of laser diagnostics to thermal power plants and engines," *Appl. Therm. Eng.,* vol. 73, pp. 1453-1464, 2014.

[77] Y. Deguchi, T. Kamimoto, Y. Kiyota, "Time resolved 2D concentration and temperature measurement using CT tunable laser absorption spectroscopy," *Flow Meas. Instrum.,* vol. 46, p. 312, 2015.

[78] T. Kamimoto, Y. Deguchi, N. Zhang, R. Nakao, T. Takagi, and J. Z. Zhang, "Real-time 2D Concentration Measurement of CH4 in Oscillating Flames Using CT Tunable Diode Laser Absorption Spectroscopy," *J. Appl. Nonlinear Dyn.,* vol. 4, pp. 295-303, 2015.

[79] T. Kamimoto, Y. Deguchi, D. W. Choi, J. H. Shim, "Validation of the real-time 2D temprature meaurement method using the CT tunable diode laser absorption spectroscopy," *Heat Transfer Res.,* vol. 47, p. 193, 2016.

[80] D. W. Choi, M. G. Jeon, G. R. Cho, T. Kamimoto, Y. Deguchi, and D. H. Doh, "Performane Improvements in Temperature Reconstructions of 2-D Tunable Diode Laser Absorption Spectroscopy (TDLAS)," *J. Therm. Sci.,* vol. 25, p. 84, 2016.

[81] M. G. Allen, "Diode laser absorption sensors for gas-dynamic and combustion flows," *Meas. Sci. Technol.,* vol. 9, p. 545, 1998.

[82] C. Liu, L. Xu, J. Chen, Z. Cao, Y. Lin, and W. Cai, "Development of a fan-beam TDLAS-based tomographic sensor for rapid imaging of temperture and gas concentration," *Opt. Express,* vol. 23, p. 22494, 2015.

[83] P. Sun, Z. Zhang, Z. Li, Q. Guo, and F. Dong, "Study of Two Dimensional Tomography Reconstruction of Temperature and Gas Concentration in a Combustion Field Using TDLAS," *Appl. Sci.,* vol. 7, p. 990, 2017.

[84] H. Shinohara, K. Nakaseko, K. Sakaguchi, and T. Hashimoto, Chikujikinnji gazousaikousei no kiso, Iryokagaku-sha, 2013, in Japanese.

[85] Y. Deguchi, M. Noda, M. Abe, and M. Abe, "Improvement of combustion control through real-time measurement of O2 and CO concentrations in incinerators using diode laser absorption spectroscopy," *Proc. Combust. Inst.,* vol. 29, p. 147, 2002.

[86] L.S. Rothman et al, "The HITRAN 2008 molecular spectroscopic database," *J. Quant. Spect. Radiat. Trans.,* vol. 110, p. 533, 2009.

Acknowledgment

The author gratefully acknowledge Prof. Yoshihiro Deguchi, Graduate School of Advanced Technology and Science, The University of Tokushima, for his sincere guidance, support and encouragements throughout the study.

The author is deeply thankful Dr. Hitoshi Iida, The University of Tokushima, for his efforts to develop the data acquisition software. The author is thankful Dr. Takahiro Kamimoto and students in the Laser&Plasma Laboratory, The Tokushima University, for the cooperation regarding the assemble of the experimental setup and construction of the CH_4 spectrum database.

The author express especial appreciations to colleagues in HORIBA STEC, Co., Ltd., Dr. Kiyoaki Hara, Fellow of the Research & Development of HORIBA STEC, Co., Ltd., Mr. Seiji Usui, Executive Managing Director, Mr. Hiroshi Kawano, Corporate Officer, Mr. Masaki Inoue, Director of the Fukuchiyama Technology Center, and Mr. Masakazu Minami, Chief Director of Development Dept. 3, for their frequent encouragements and significant advices. The author is grateful Mr. Shoji Narukami and Mr. Junya Nakai, Research & Development Dept. 3, HORIBA STEC, Co., Ltd., for their cooperation on designing the experimental semiconductor chamber and the simulation of computer fluid dynamics. The author wish to thank Mr. Andrew Price, HORIBA STEC, Co., Ltd., and Mr. Jeffery Ransdell, HORIBA Instruments Incorporated, for their cooperation on the check of the English expressions.